


Tensorial stress-plastic strain fields in α - ω Zr mixture, transformation kinetics, and friction in diamond-anvil cell

Received: 7 February 2023

Valery I. Levitas^{1,2,3,5}✉, Achyut Dhar^{1,5}✉ & K. K. Pandey⁴

Accepted: 14 September 2023

Published online: 23 September 2023

 Check for updates

Various phenomena (phase transformations (PTs), chemical reactions, microstructure evolution, strength, and friction) under high pressures in diamond-anvil cell are strongly affected by fields of stress and plastic strain tensors. However, they could not be measured. Here, we suggest coupled experimental-analytical-computational approaches utilizing synchrotron X-ray diffraction, to solve an inverse problem and find fields of all components of stress and plastic strain tensors and friction rules before, during, and after α - ω PT in strongly plastically predeformed Zr. Results are in good correspondence with each other and experiments. Due to advanced characterization, the minimum pressure for the strain-induced α - ω PT is changed from 1.36 to 2.7 GPa. It is independent of the plastic strain before PT and compression-shear path. The theoretically predicted plastic strain-controlled kinetic equation is verified and quantified. Obtained results open opportunities for developing quantitative high-pressure/stress science, including mechanochemistry, synthesis of new nanostructured materials, geophysics, astrogeology, and tribology.

In static high-pressure studies, high pressures are generated by compression, with large very-heterogeneous elastoplastic deformations, of a thin sample down to 6–20 microns in a diamond-anvil cell (DAC)^{1–7}; see Fig. 1a. The same happens when the pressure-transmitting medium solidifies (Supplementary Fig. 12). We will focus here on stresses and plastic strains averaged over the polycrystalline aggregate rather than in individual grains. The most advanced characterization of the pressure conditions in a sample is based on determining the radial distribution of pressure averaged over the sample thickness using the volume of a crystal cell measured by X-ray diffraction (XRD) and equation of state (EOS) determined under hydrostatic conditions^{4,5,8–11}. However, EOS for hydrostatic and non-hydrostatic loadings are quite different^{12–15}. More importantly, for the XRD beam along the symmetry axis of the DAC (axial XRD), crystallographic planes that are almost parallel to

the beam contribute to the measured XRD patterns only, and axial elastic strain $\bar{E}_{0,zz}$ and consequently stress $\bar{\sigma}_{zz}$ do not contribute to the pressure, leading to large error (bar over the field variables means averaged over the sample thickness). In addition, numerous physical, chemical, geological, and mechanical problems and phenomena are related to knowledge of the fields of all components of the stress, elastic, and plastic strain tensors in materials compressed in DAC^{1–7,11–13,16–31}. For example, contact friction shear stress between diamond and sample/gasket is responsible for generating high pressure and is the key boundary condition for simulation of the processes in DAC;^{1,4–6,21,32–39} however, the friction rules are unknown. It is known that phase transformations (PTs) and chemical reactions strongly depend on the non-hydrostatic stresses and plastic strains^{11,16,20,22,23,26–31,40,41}, even within different pressure-transmitting media at relatively low pressure^{24,42}. New types, namely plastic

¹Department of Aerospace Engineering, Iowa State University, Ames, IA 50011, USA. ²Department of Mechanical Engineering, Iowa State University, Ames, IA 50011, USA. ³Ames National Laboratory, Division of Materials Science and Engineering, Ames, IA 50011, USA. ⁴High Pressure & Synchrotron Radiation Physics Division, Bhabha Atomic Research Centre, Bombay, Mumbai 400085, India. ⁵These authors contributed equally: Valery I. Levitas, Achyut Dhar.

✉ e-mail: vlevitas@iastate.edu; adhar@iastate.edu

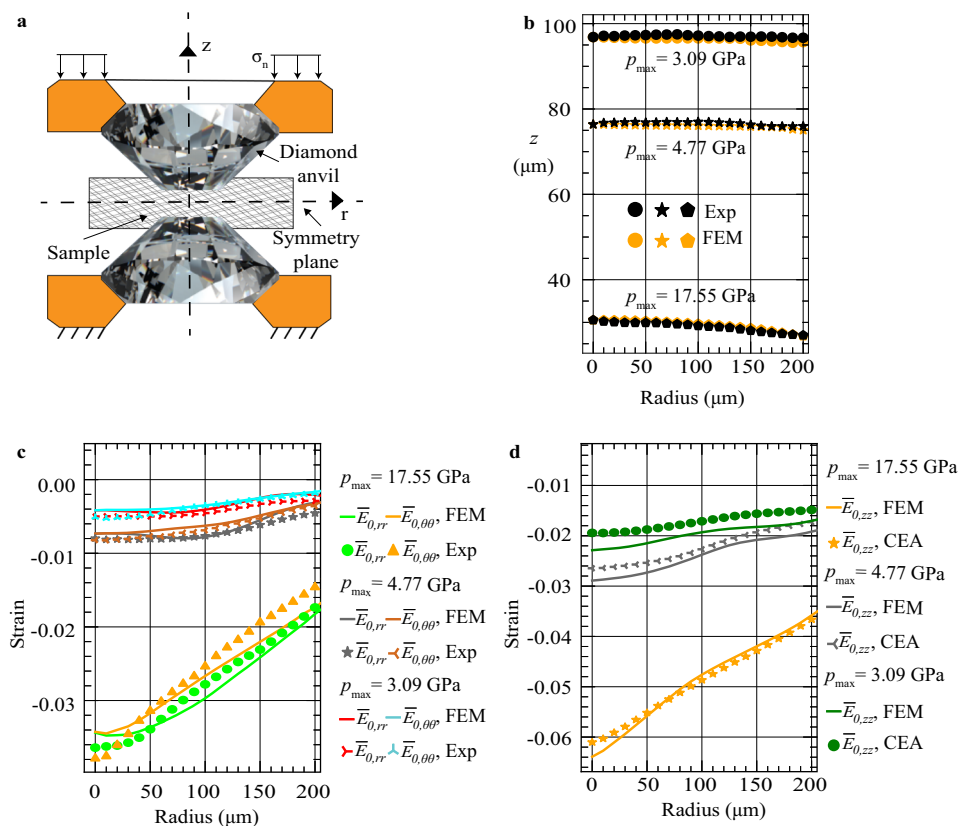


Fig. 1 | Distributions of different strains in DAC. a DAC schematic. **b** The sample thickness profiles from the X-ray absorption and FEM. **c** Comparison of experimental and FEM results for distributions of elastic radial $\bar{E}_{0,rr}(r)$ and the hoop

$\bar{E}_{0,\theta\theta}(r)$ strains in a mixture averaged over the sample thickness. **d** Comparison of FEM and CEA distributions of elastic axial strains $\bar{E}_{0,zz}$.

strain-induced PTs and reactions were formulated and are under intense studies^{11,23,40,43}. Plastic strain can reduce PT pressure in comparison with quasi-hydrostatic experiment from more than 52.5 to 6.7 GPa for rhombohedral to cubic BN²⁷, from 55 to 5.6 GPa for hexagonal to superhard wurtzitic BN²⁰, and from 70 to 0.7 GPa for graphite to cubic diamond²², which may lead to new technologies. Also, the plastic strain may lead to new nanostructured phases that could not be obtained under hydrostatic conditions, substitute time-dependent kinetics with fast plastic strain-dependent kinetics, and substitute reversible PTs with irreversible PTs that allow one to use retrieved phases in engineering applications^{11,22,23,27,28,40}. Severe plastic deformation with high-pressure torsion⁴⁴ is an example of the realization of such technologies. Strain-induced PTs under high pressure also occur during surface processing (polishing, turning, scratching, etc.) of strong brittle semiconductors and ceramics and are utilized for developing regimes of ductile machining⁴⁵. Again, since stress and plastic strain tensors are not measurable, quantitative studies of these phenomena are impossible.

The paper that claims measurement of radial distribution of all components of the stress tensor is ref. 46. However, this measurement is performed in a diamond culet rather than in a sample, which gives boundary normal and shear stresses at the sample boundary only instead of full stress and plastic strain tensor fields in the entire sample. Since there was a problem in the precise measurement of the shear stress, finite element method (FEM) simulation was utilized to supplement the experiment. In ref. 35, all tensorial fields are determined in the polycrystalline W sample; however, input data are the radial pressure distributions determined using EOS. Measured displacements of material particles at the contact surface with diamond²⁷ represent important boundary conditions, which still were not connected to FEM simulations.

Here, we develop coupled experimental-analytical (CEA) and CEA-FEM approaches for solving an inverse problem of determining fields of all stress, elastic and plastic strain components (in each phase and in the mixture), and friction shear stress before, during, and after α - ω PT in commercially pure polycrystalline Zr, see flowchart in Supplementary Fig. 1. Importantly, to exclude the effect of strain hardening, change in grain size and dislocation density, and their effect on the thermodynamics and kinetics of PT, we have strongly preliminary deformed Zr until its hardness does not change^{11,34}; grain size and dislocation density in pure α - and ω -Zr do not change with further straining as well⁴⁷. This is a crucial step to make the problem solvable. Next, based on limited access of the beam for axial geometry, determined fields of XRD patterns, and texture of both phases, we concluded that the most informative and precise approach is to determine, through postprocessing, distributions of the elastic radial $\bar{E}_{0,rr}(r)$ and hoop $\bar{E}_{0,\theta\theta}(r)$ strains in α and ω phases. Sample thickness profile and pressure-dependence of the yield strength of phases are determined using X-ray absorption^{4,5,11} and broadening of X-ray peaks^{11,48}. The CEA approach is developed to determine friction shear stress and all components of stress and elastic strain tensors in each phase and mixture of phases based on XRD measurements. Next, using found friction stress, detailed FEM modeling, and simulation are performed that determine all components of stress and plastic strain tensors, which completes the problem in the CEA-FEM approach. Remarkably, the results of analytical and FEM solutions for all stresses are in good correspondence. Distributions of $\bar{E}_{0,rr}(r)$, $\bar{E}_{0,\theta\theta}(r)$ and sample thickness profiles calculated with FEM perfectly correspond to experiments. Obtained pressure distribution differs significantly from that using the EOS-based method. The corrected minimum pressure for the strain-induced α - ω PT is $p_{\min}^d = 2.70$ GPa vs. 1.36 GPa based on the EOS method. Still, it is smaller than under hydrostatic loading by a

factor of 2 (and smaller than the phase equilibrium pressure by a factor of 1.3); it is found to be independent of the plastic strain tensor and its path, in particular, of the compression-shear strain path. The theoretically predicted plastic strain-controlled kinetic equation was verified and quantified; it is independent of the plastic strain at pressures below p_e^d and the pressure-plastic strain loading path. Based on our texture analysis (see Supplementary Notes), *c* axis of α -Zr is predominantly aligned along the loading direction; however, *c* axis of ω -Zr is predominantly aligned along the radial direction. In addition, based on the analysis of the XRD peak broadening⁴⁸, we obtained the yield strength of α -Zr $\sigma_y^\alpha = 0.82 + 0.190p$ (GPa) and ω -Zr $\sigma_y^\omega = 1.66 + 0.083p$ (GPa) (Supplementary Fig. 9).

Results

Results for three different loadings identified by averaged over the thickness pressure in the mixture \bar{p} at the symmetry axis (i.e., maximum pressure p_{max}) are presented in Fig. 1. The loadings with $p_{max} = 3.09$ GPa is for the almost pure α -Zr phase, for $p_{max} = 4.77$ GPa is for the mixture of α - and ω -Zr, and for $p_{max} = 17.55$ GPa is for the pure ω -Zr phase. The corresponding volume fraction profiles $c(r)$ are shown at the bottom of Fig. 2. The sample thickness profiles from the X-ray absorption and FEM are in good correspondence (Fig. 1b). There is also good correspondence between experiments and FEM distributions of $\bar{E}_{0,rr}(r)$ and $\bar{E}_{0,\theta\theta}(r)$, as well as the closeness of $\bar{E}_{0,rr}(r)$ to $\bar{E}_{0,\theta\theta}(r)$ (Fig. 1c). Both experimental verifications of FEM results represent nontrivial validation of the model and simulations; thus, all FEM fields presented below represent reality, even if they cannot be directly measured. Figure 1d shows good correspondence between FEM and CEA distributions of the elastic axial strains $\bar{E}_{0,zz}(r)$, which is a part of the validation of the analytical model.

The comparison of different radial stress distributions obtained with FEM and CEA is given in Fig. 2. The practical coincidence of the contact friction stress τ_c from CEA and FEM is not surprising because the field $m(r)$ from the analytical solution is used in FEM as the

boundary condition. All stresses smoothly increase from the edge of a culet to the sample center. For all three loadings, there is a very good, and for some stresses, excellent correspondence between the analytical and the FEM results. In addition, FEM distributions of σ_{zz}^c at the contact surface and σ_{zz}^{sp} at the symmetry plane do not differ essentially, which supports the assumption in the analytical model that σ_{zz} is independent of *z*. It can also be seen that $\sigma_{rr} \approx \sigma_{\theta\theta}$ from FEM at the symmetry plane, contact surface, and averaged over the thickness, which justifies the assumption $\sigma_{rr} = \sigma_{\theta\theta}$ made in the analytical model. Comparison of 2D stress contours obtained with CEA and FEM approaches is presented in Supplementary Fig. 11. Maximum values of the same stresses are practically the same, character of changes of all stresses is also the same, i.e., correspondence is good. Thus, despite the simplicity and numerous assumptions, the analytical model describes well stress fields from FEM, and can be used for analysis and interpretation of experiments. Friction shear stress is essentially lower than the yield strength for all pressures. That means that the known method^{6,21,32} to determine the yield strength in shear based on the equilibrium Eq. (59) (see Supplementary Notes) and assumption $m = 1$ does not work. From the edge toward the center, friction stress grows, reaches the maximum and then reduces to zero at the center of a sample due to symmetry conditions.

Friction laws can be formalized with the following equations (Supplementary Fig. 8):

$$\begin{aligned} \left(\frac{\tau_c}{\tau_y}\right)_\omega &= 0.186 + 0.018p^c & \text{for } 11.1 \leq p^c(\text{GPa}) \leq 15.0; & \quad 60 \leq r(\mu\text{m}) \leq 140 \\ \left(\frac{\tau_c}{\tau_y}\right)_{\alpha+\omega} &= -0.179 + 0.241p^c & \text{for } 2.7 \leq p^c(\text{GPa}) \leq 3.7; & \quad 130 \leq r(\mu\text{m}) \leq 200 \\ \left(\frac{\tau_c}{\tau_y}\right)_\alpha &= -1.282 + 0.722p^c & \text{for } 2.0 \leq p^c(\text{GPa}) \leq 2.45; & \quad 130 \leq r(\mu\text{m}) \leq 190. \end{aligned} \tag{1}$$

The radial distributions of averaged through thickness pressure in α -Zr \bar{p}^α are shown in Fig. 3a. They are obtained using a developed

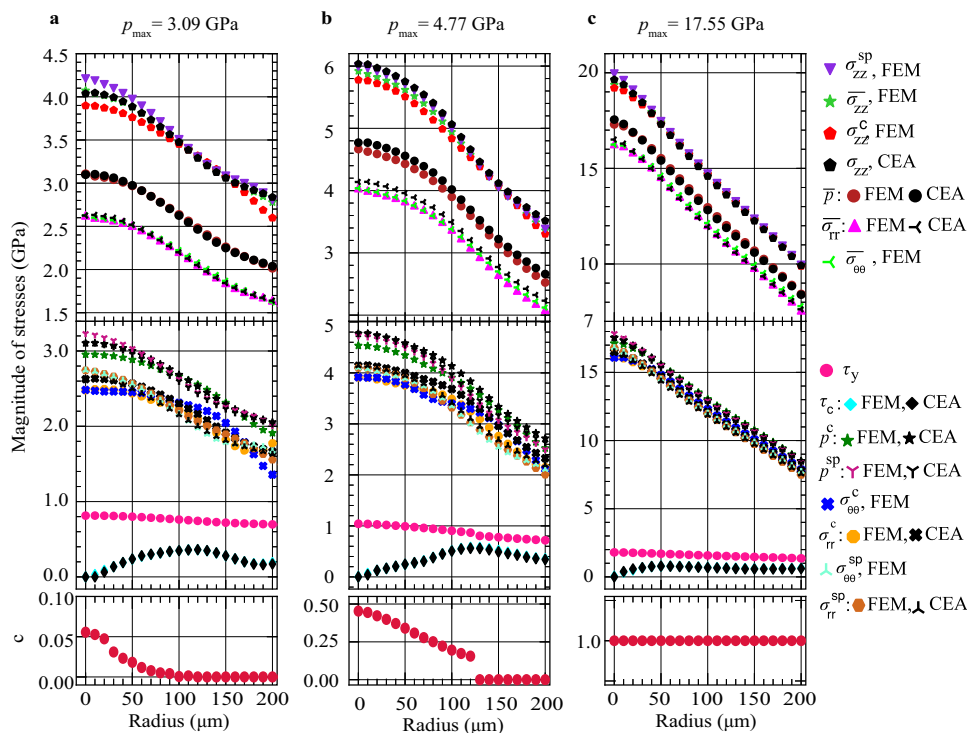


Fig. 2 | Comparison of different radial stress distributions obtained with FEM and analytically. **a** Results for almost pure α -Zr at $p_{max} = 3.09$ GPa. **b** Results for mixture of α - and ω -Zr at $p_{max} = 4.77$ GPa. **c** Results for pure ω -Zr at

$p_{max} = 17.55$ GPa. Distributions of the volume fraction $c(r)$ for the corresponding loadings are shown at the bottom of the figure. Subscripts 'c' and 'sp' mean contact surface and symmetry plane, respectively.

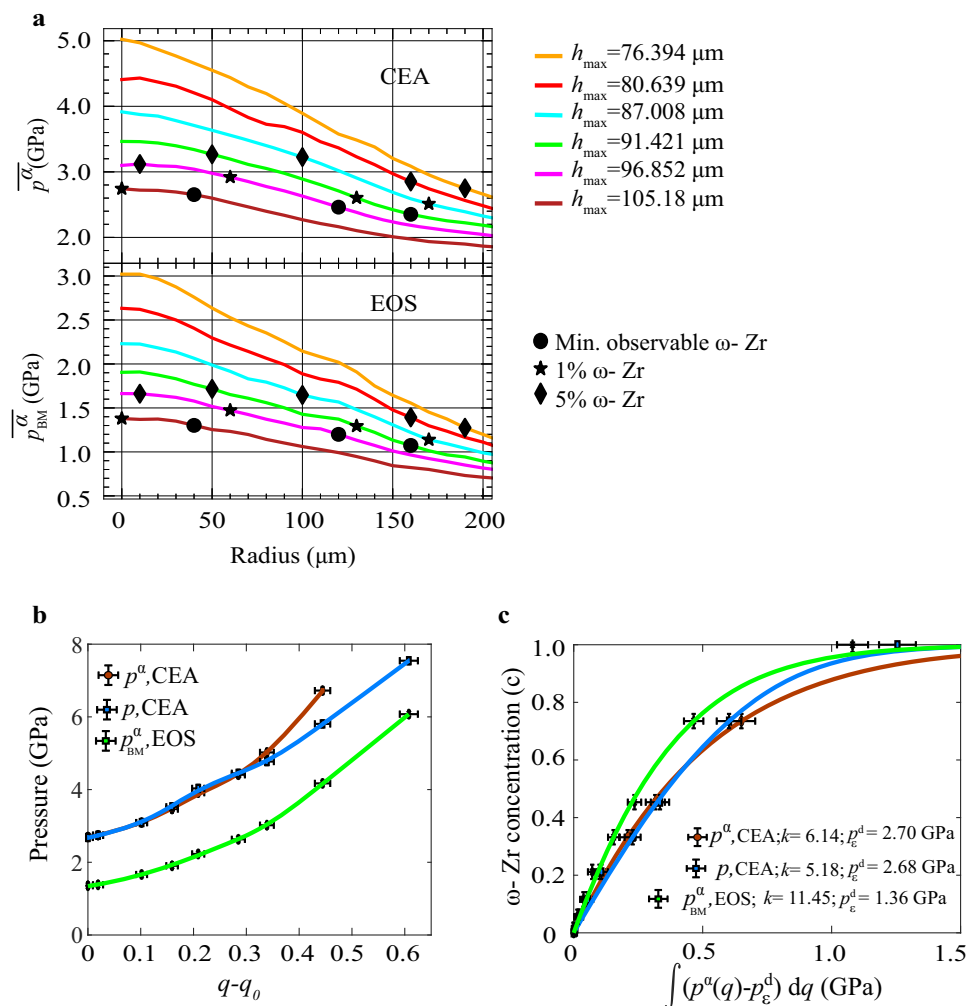


Fig. 3 | Kinetics of α - ω PT. **a** The radial distribution of \bar{p}^α in α -Zr obtained using developed CEA based on experimentally measured radial $\bar{E}_{0,rr}(r)$ and the hoop $\bar{E}_{0,\theta\theta}(r)$ strains (top) and hydrostatic EOS based on experimentally measured elastic volumetric strain, for the same sample thicknesses. Three types of markers are superposed on these curves corresponding to $c = 0.05, 0.01$, and minimum observable traces of $\omega - \text{Zr}$. **b** Loading pressure-accumulated plastic strain paths. Error in the estimation of q is based on the error in estimation of thickness which is 1 micron. Error in the estimation of pressure of 0.2 GPa is based on the error in

estimation of lattice parameters. **c** Corresponding kinetics of evolution of $\omega - \text{Zr}$ concentration based on pressures in the parent α -Zr obtained using CEA and EOS, as well as averaged over the mixture pressure obtained with the CEA; lines correspond to Eq. (2). Here q_0 is the accumulated plastic strain at the beginning of PT. Error in $\int (p(q) - p_\epsilon^d) dq$ is evaluated based on the convolution of errors in estimating the pressure and the q . Error in the estimation of concentration of 0.05 is based on fitting XRD with 2 phases.

approach (top) and using hydrostatic (bottom), for the same sample thicknesses. It is evident that the suggested CEA approach to post-process X-ray measurements leads to pressures higher by a factor of 1.7–2.0 or by 1.4–2.0 GPa (i.e., at the level of the yield strength σ_y at the corresponding pressure) than those obtained by traditional utilization of EOS. This is a quite significant correction that should be applied to all previous publications in pressure measurements based on EOS^{4,5}.

The obtained corrections also lead to a reinterpretation of the kinetics of α - ω PT in comparison with that in¹¹. The strain-controlled kinetic equation derived in ref. 23 and simplified for Zr in ref. 11 is

$$\frac{dc}{dq} = k(1 - c) \frac{p(q) - p_\epsilon^d}{p_h^d - p_\epsilon^d} \rightarrow c = 1 - \exp\left(\frac{-k}{(p_h^d - p_\epsilon^d)} \int (p(q) - p_\epsilon^d) dq\right) \quad (2)$$

where p is pressure either in mixture or in α -Zr (\bar{p}^α), q is the accumulated plastic strain, p_h^d is the pressure for initiation of pressure-induced PT under hydrostatic loading, p_ϵ^d is the minimum pressure for initiation of the plastic strain-induced PT, $p(q)$ is the loading path. To quantify Eq. (2), experimental points at the center of the sample are

used, where unidirectional compression is realized, $q = \ln(h_0/h)$, where h_0 and h are the initial and current sample thicknesses at the center. For strongly plastically pre-deformed Zr we found that $p_h^d = 5.4$ GPa. Figure 3b shows the experimental loading path $p(q)$ based on different pressures: pressures in the parent α -Zr obtained using an analytical model and EOS, as well as averaged over the mixture pressure obtained with an analytical model. The loading path with the analytical model is shifted up with respect to the EOS-based model by 1.3–2.0 GPa. To detect the initiation of PT, three types of markers are superposed on the pressure distribution curves corresponding to $c = 0.05, 0.01$, and minimum observable traces of $\omega - \text{Zr}$. The minimum pressure for initiation of the plastic strain-induced PT is determined by extrapolating p - c results to $c = 0$ at the sample center, which gives $p_\epsilon^d = 2.70$ GPa with CEA approach instead of $p_\epsilon^d = 1.36$ GPa based on EOS. Thus, the developed method led to an essential increase in the minimum PT pressure. Still, it is two times lower than under hydrostatic conditions and lower than the phase equilibrium pressure of 3.4 GPa. Note that with the EOS method, p_ϵ^d here for commercially pure Zr is slightly higher than 1.2 GPa for ultra-pure Zr in ref. 11. It is important that for both methods of pressure determination, all three

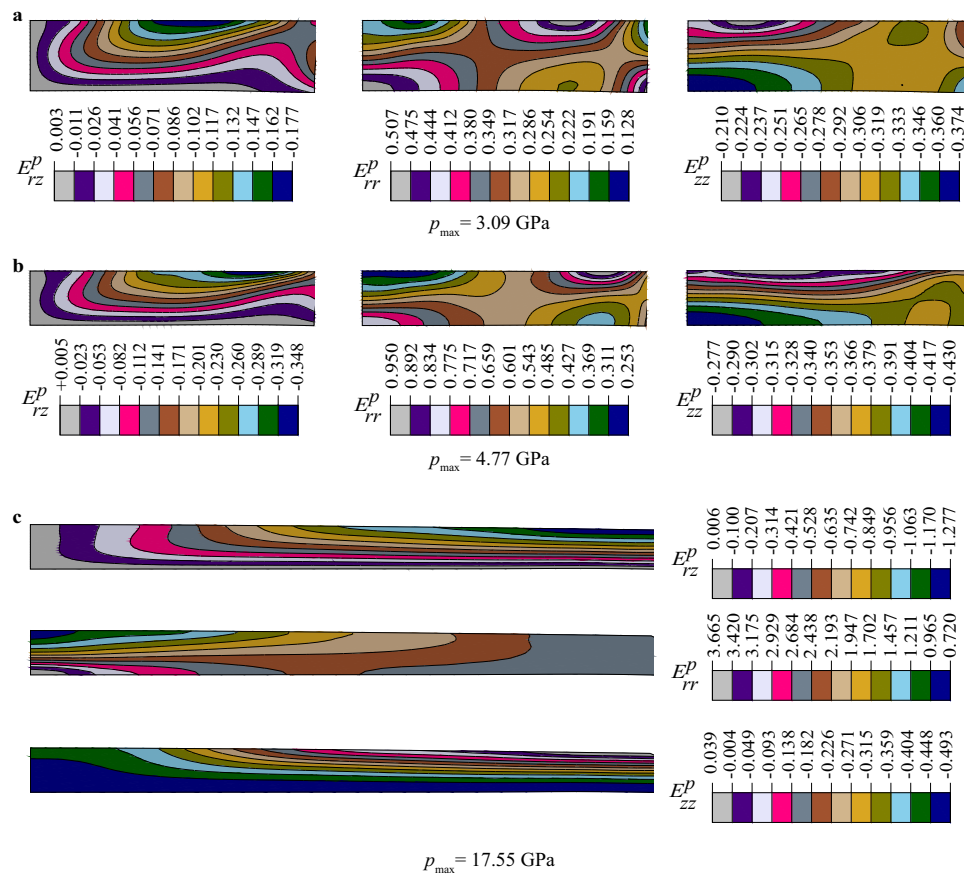


Fig. 4 | Distributions of components of Lagrangian plastic strains in a sample for three loadings. **a** Results for almost pure α -Zr at $p_{\max} = 3.09$ GPa. **b** Results for mixture of α - and ω -Zr at $p_{\max} = 4.77$ GPa. **c** Results for pure ω -Zr at $p_{\max} = 17.55$ GPa.

types of markers in Fig. 3a show very close values for different radii, i.e., the minimum PT pressure is practically independent of r . However, the plastic strain tensor and its path are very different for different radii. At the center, unidirectional compression without shear takes place while with increasing radius shear strain grows. Consequently, p_{ε}^d is independent of the plastic strain tensor and its path, in particular, of compression/shear plastic strain state and its path. This means that there is no advantage of shear deformation mode in promoting PTs, physical mechanisms are the same for PT under plastic compression and under shear, and PT processes under compression in DAC and torsion in rotational DAC require the same experimental characterization and theoretical treatment. However, rotational DAC allows to independently control pressure and plastic strain and produces PT up to completion close to p_{ε}^d , which is also important for technologies of plastic strain and defect-induced material synthesis at relatively low pressure.

Experimental points for PT kinetics based on three different pressures are well described by Eq. (2) with different p_{ε}^d and kinetic coefficients k , see Fig. 3c. This validates Eq. (2) for a quite nontrivial loading path. While the difference between kinetic curves with pressures based on the CEA approach and EOS does not look drastic, this is due to the choice of independent variables along the horizontal axis, different for different cases. Quantitatively, the CEA method led not only to an increase in p_{ε}^d by a factor of 2 but also to a decrease in kinetic coefficient k from 11.45 to 6.14, i.e., correction is very significant. Since this correction did not change the conclusion that p_{ε}^d is independent of compression/shear plastic strain state and its path, we assume that other conclusions from¹¹, that Eq. (2) is independent of the magnitude of plastic strain q_0 below p_{ε}^d and of $p - q$ loading path, are valid as well.

Fields of all components of Lagrangian plastic strain tensor found with the CEA-FEM approach are presented in Fig. 4. Very heterogeneous and nontrivial distributions are observed, caused by heterogeneous contact friction. These fields will be used in future work, which will include simulation of the strain-induced PT as well, to derive, calibrate, and validate a more precise kinetic equation for strain-induced PT.

To summarize, we developed coupled CEA and CEA-FEM approaches that allow us to solve the inverse problem reinterpret X-ray diffraction measurements, and determine pressure and tensorial stress-plastic strain fields in each phase and mixture, as well as contact friction rules in a DAC before, during, and after α - ω transformation in Zr. Good correspondence of the elastic radial $\bar{E}_{0,rr}(r)$ and hoop $\bar{E}_{0,\theta\theta}(r)$ strains and the sample thickness profile between FEM and experiments and the stress tensor fields between the CEA approach and FEM validates the developed approach. Due to advanced characterization, the minimum pressure p_{ε}^d for the strain-induced α - ω PT in Zr is changed from 1.36 to 2.7 GPa and the kinetic coefficient k is reduced from 11.45 to 6.14, i.e., correction is very significant. Still, p_{ε}^d is 2 times lower than under hydrostatic conditions and lower than the phase equilibrium pressure of 3.4 GPa. The found independence of p_{ε}^d of the plastic strain tensor and its path (in particular, compression-shear path) means basic equivalence of PT processes under compression in DAC and torsion in rotational DAC. However, rotational DAC allows to independently control pressure and plastic strain and produces PT up to completion at pressures close to p_{ε}^d , which is important for technologies of plastic strain and defect-induced material synthesis at relatively low pressure. Since our pressure correction did not change the conclusion that p_{ε}^d is independent of compression/shear plastic strain state and its path, it is highly probable that other conclusions from¹¹, that kinetic Eq. (2) is

independent of the magnitude of plastic strain q_0 below p_ε^d and of p - q loading path, are valid as well.

The obtained results in this work open opportunities for developing quantitative high-pressure/stress science. The same methods are applicable for other material systems (including gasket materials), for sample-gasket systems, without and with hydrostatic medium, after its solidification, and can be extended for processes in rotational DAC (Supplementary Fig. 12). They can significantly improve the accuracy of pressure field determination and characterization of all processes studied under pressure: physical, chemical, biological, geophysical, and others. Finding fields of stress tensor components (which can be done using analytical model) will allow quantifying their effect on the processes under study, instead of referring to the qualitative effect of pressure-transmitting media and “non-hydrostatic” stresses. Finding fields of plastic strain tensor components, that cannot be measured, will allow us to quantitatively study plastic strain-induced PTs and chemical reactions and initiate quantitative high-pressure mechanochemistry. This may lead to new technologies of plastic strain and defect-induced material synthesis at relatively low pressure, in particular, for diamond²² and cubic BN^{20,27}, initiation of high-pressure tribology, explanation of deep-focus earthquakes²⁹, the appearance of microdiamond in the low pressure and temperature Earth’s crust²², and mechanochemical origin of life in the icy crust of solar system’s moons and planets^{30,31}. Our method generates big data from single experiments/simulation, which can be utilized for machine learning-based development and calibration of the corresponding constitutive equations. Thus, the main challenge, namely, strong heterogeneity of all fields, can be transformed into an opportunity.

Methods

CEA approach

Two mechanical equilibrium equations for the axisymmetric model in radial r and axial z directions, the pressure-dependent *von-Mises* yield equation for isotropic perfectly plastic polycrystal $(\frac{3}{2}S_{ij}S_{ij})^{0.5} = \sigma_y = (1 - c)\sigma_y^\alpha(p) + c\sigma_y^\omega(p)$, and the assumption that radial stress σ_{rr} is equal to azimuthal stress $\sigma_{\theta\theta}$, i.e. $\sigma_{rr} = \sigma_{\theta\theta}$, form 4 equations with four unknown stresses, σ_{rr} , $\sigma_{\theta\theta}$, axial σ_{zz} , and shear stress $\tau = \tau_{rz}$. Here, σ_y is the yield strength in compression of the mixture, c is the volume fraction of ω -Zr, and S_{ij} are components of the deviatoric stress tensor in the mixture. An approximate analytical solution to this statically determined system of equations is found by modifying the Prandtl solution for the plane strain (see Supplementary Notes, Section 2). However, it depends on unknown contact friction shear stress $\tau_c = m\tau_y(p, c)$, where $\tau_c = \frac{\sigma_y(p, c)}{\sqrt{3}}$ is the yield strength in shear of the mixture and m is the factor to be determined. To find the distribution of the friction stress in terms of measured contribution of elastic strain averaged over the sample thickness $\bar{E}_{0,rr}(r) \approx \bar{E}_{0,\theta\theta}(r)$, i.e., in terms of $0.5(\bar{E}_{0,rr}(r) + \bar{E}_{0,\theta\theta}(r))$, the equations derived in (see Supplementary Notes, Section 2) are used.

The modified Hooke’s law for hydrostatically pre-stressed properly oriented α - and ω -Zr single crystals with determined pressure-dependent elastic moduli is used to determine stresses in each phase and mixture (see Supplementary Notes). Then both Hooke’s law and stress fields from the modified Prandtl solutions are averaged over the sample thickness for each r . The *Reuss* hypothesis is used that stresses in a mixture of all α - and ω -Zr single crystals in the representative volume and in polycrystalline aggregate (that participate in the modified Prandtl solution) are the same. This hypothesis appears to work well due to the highly textured polycrystalline aggregate. Finally, the simplified mechanical equilibrium equation averaged over the sample thickness is utilized, to determine the contact friction shear stress. After the solution of the obtained nonlinear system of algebraic/trigonometric equations for $m(r)$ and \bar{p} , all components of the fields of

stress and elastic strain tensors in each phase and mixture of phases are obtained analytically, but plastic strains are unknown.

FEM modeling and simulations

A large elastoplastic strain model for mixture of α - and ω -Zr using the mixture rule for all properties is advanced (see Supplementary Notes). The evolution of the field of the measured volume fraction of ω -Zr $c(r)$ and corresponding isotropic transformation strain are introduced homogeneously along the z coordinate. Obtained analytically evolution of the field $m(r)$ is used as the boundary condition for the contact problem in the culet portion. At the inclined portion of the sample-anvil contact surface, the contact shear stress is determined by the minimum between $\tau_c = m\tau_y(p)$, with the value of m at the culet-inclined surface boundary, and Coulomb friction. The elastic constitutive response of polycrystalline Zr is modeled using 3rd-order Murnaghan potential. Associated flow rule in deviatoric stress space is used along with plastic incompressibility. The elastic response of the diamond is modeled using 4th order elastic potential for cubic crystal averaged over azimuthal direction to keep the axial symmetry.

Materials

The material studied in the paper is the same as was used by Zhilyaev et al.⁴⁹, purchased from Haines and Maassen (Bonn, Germany), i.e., commercially pure (99.8%) α -Zr (Fe: 330 ppm; Mn: 27 ppm; Hf: 452 ppm; S: <550 ppm; Nd: <500 ppm). The sample slab with initial thickness of 5.25 mm was cold rolled down to -165 μm to obtain plastically pre-deformed sample with saturated hardness. Vickers microhardness test method was used to characterize the hardness of the sample at several steps during cold rolling. A 3 mm diameter disk was punch cut from thus obtained thin rolled sheet for unconstrained compression experiments in DAC. For hydrostatic compression experiments, small specks of -20 μm size were chipped off from the plastically pre-deformed sample using the diamond file.

The hydrostatic high-pressure X-ray diffraction measurements were carried out using the same DAC to estimate equation of state, bulk modulus, and its pressure derivative at ambient pressure for this sample. For these experiments, small Zr specks of -20 μm size, as already mentioned, were loaded in sample chamber along with silicone oil and copper chips as pressure-transmitting medium and pressure marker respectively. The sample chamber was prepared by drilling a hole of -250 μm diameter in steel gaskets pre-indented using diamond anvils from initial thickness of -250 μm to -50 μm . Hydrostatic high-pressure experiments were carried out in small pressure steps of -0.2 GPa up to a maximum pressure of 16 GPa.

Experimental techniques and methodology

Unconstrained plastic compression experiments were carried out prescribing different compression loads to plastically pre-deformed Zr sample loaded in DAC without any constraining gasket. The sample was subjected to axial loads of 50 N, 100 N, 150 N, 170 N, 190 N, 210 N, 230 N, 250 N, 270 N, 290 N, 310 N, 330 N, 350 N, 400 N, 450 N, 500 N, 550 N, 600 N, 650 N, 700 N, 750 N, 800 N, 850 N, 900 N, 950 N, and 1000 N.

In situ XRD experiments were performed at 16-BM-D beamline at HPCAT sector at Advanced Photon Source employing focused monochromatic X-rays of wavelength 0.3096(3) \AA and size -6 μm \times 5 μm (full-width at half maximum). At each load-condition, the sample was radially scanned over the entire culet diameter (500 μm) in steps of 10 μm , and 2D diffraction images were recorded at Perkin Elmer flat panel detector. At each load step, X-ray absorption scan was also recorded in same 10 μm steps to obtain thickness profile of sample under given load condition.

2D diffraction images were converted to a 1D diffraction pattern using FIT2D software^{50,51} and subsequently analyzed through Rietveld refinement^{52,53} using GSAS II⁵⁴ and MAUD⁵⁵ software for obtaining

lattice parameters, phase fractions, and texture parameters of both α and ω phases of Zr. Based on the different angular dependence of the grain size and microstrain contributions to the diffraction peak broadening, they can be separated. The whole powder pattern fitting using the modified Rietveld method (as implemented in MAUD software⁵⁶) was utilized, which takes texturing and stress anisotropy into account.

In axial geometry (i.e., when the incident X-ray beam is directed along z axis) (Supplementary Figs. 1a and 10), the diffraction condition is satisfied mostly for those crystallographic planes that are nearly parallel (plane normal perpendicular) to the load axis. Hence the observed shifts in diffraction peaks can be practically used to estimate strains in radial and azimuthal directions viz. $\bar{E}_{0,11} = \bar{E}_{0,rr}$ and $\bar{E}_{0,22} = \bar{E}_{0,\theta\theta}$ averaged over the sample thickness. Ideally, the angle between the load axis and diffraction vector ψ should be equal to 90° to estimate these strain components. However, since this is not possible in axial geometry, we can use the diffraction peak with smallest diffraction angle, θ . In our experiments for α -Zr, (100) diffraction peak appears at $\theta = 3.18^\circ$ for used X-rays ($\lambda = 3.1088 \text{ \AA}$) at ambient pressure. This corresponds to $\psi = 86.82^\circ$ and can be used for estimation of strain components $\bar{E}_{0,rr}$ and $\bar{E}_{0,\theta\theta}$. Note that (100) peak corresponds to a' lattice parameter because c -axis of α -Zr is predominantly aligned along the loading direction as per our texture analysis.

For ω -Zr, (001) diffraction peak appearing at $\theta = 2.85^\circ$ ($\psi = 87.15^\circ$) can be used for estimation of strain components $\bar{E}_{0,rr}$ and $\bar{E}_{0,\theta\theta}$. The (001) peak of ω -Zr corresponds to c' lattice parameter and as per texture analysis, c axis of ω -Zr is predominantly perpendicular to the loading direction of DAC.

Thus, strain components $\bar{E}_{0,rr}$ and $\bar{E}_{0,\theta\theta}$ for α and ω phases of Zr have been obtained for each loading condition at each scanning position using the following equations:

For α -Zr:

$$\bar{E}_{0,rr} = 0.5 \left((a/a_0)^2 - 1 \right) \text{ using } \phi = 0^\circ \text{ sector of (100) diffraction ring;}$$

$$\bar{E}_{0,\theta\theta} = 0.5 \left((a/a_0)^2 - 1 \right) \text{ using } \phi = 90^\circ \text{ sector of (100) diffraction ring;}$$

For ω -Zr:

$$\bar{E}_{0,rr} = 0.5 \left((c/c_0)^2 - 1 \right) \text{ using } \phi = 0^\circ \text{ sector of (001) diffraction ring;}$$

$$\bar{E}_{0,\theta\theta} = 0.5 \left((a/a_0)^2 - 1 \right) \text{ using } \phi = 90^\circ \text{ sector of (001) diffraction ring.}$$

Finally, diffraction data at the symmetry axis for all load conditions were used for quantitative analysis of the kinetics of plastic strain-induced α - ω phase transition in Zr, like in (ref. 11). For this purpose, the pressure in α -Zr and volume fraction of ω -Zr were estimated as a function of accumulated plastic strain q . At the symmetry axis, material experiences a unidirectional compression, for which $q = \ln(h_0/h)$, where h_0 is the initial thickness of the sample in DAC and h is the current thickness.

Data availability

Source data are provided with this paper.

References

- Mao, H. K. & Bell, P. M. High-pressure physics: sustained static generation of 1.36 to 1.72 Megabars. *Science* **200**, 1145–1147 (1978).
- Dubrovinsky, L., Dubrovinskaia, N., Prakapenka, V. B. & Abakumov, A. M. Implementation of micro-ball nanodiamond anvils for high-pressure studies above 6 Mbar. *Nat. Commun.* **3**, 1163 (2012).
- Dubrovinsky, L. et al. Materials synthesis at terapascal static pressures. *Nature* **605**, 274–278 (2022).
- Hemley, R. J. et al. X-Ray imaging of stress and strain of Diamond, Iron, and Tungsten at megabar pressures. *Science* **276**, 1242–1245 (1997).
- Li, B. et al. Diamond anvil cell behavior up to 4 Mbar. *Proc. Natl. Acad. Sci. USA* **115**, 1713–1717 (2018).
- Jeanloz, R., Godwal, B. K. & Meade, C. Static strength and equation of state of Rhenium at ultra-high pressures. *Nature* **349**, 687–689 (1991).
- Dias, R. P. & Silvera, I. F. Observation of the Wigner-Huntington transition to metallic hydrogen. *Science* **355**, 715–718 (2017).
- Jenei, Z. et al. Single crystal toroidal diamond anvils for high pressure experiments beyond 5 megabar. *Nat. Commun.* **9**, 3563 (2018).
- Dewaele, A., Loubeyre, P., Occelli, F., Marie, O. & Mezouar, M. Toroidal diamond anvil cell for detailed measurements under extreme static pressures. *Nat. Commun.* **9**, 2913 (2018).
- Ding, Y., Sun, Y., Jiang, S., Huang, X. & Cui, T. Frontier in the diamond anvil cell techniques for ultrahigh pressure generation. *J. Phys. Condens. Matter* **35**, 313002 (2023).
- Pandey, K. K. & Levitas, V. I. In situ quantitative study of plastic strain-induced phase transformations under high pressure: example for ultra-pure Zr. *Acta Mater.* **196**, 338–346 (2020).
- Duffy, T. S. et al. Lattice strains in Gold and Rhenium under non-hydrostatic compression to 37 GPa. *Phys. Rev. B* **60**, 15063 (1999).
- Merkel, S., Gruson, M., Wang, Y., Nishiyama, N. & Tomé, C. N. Texture and elastic strains in hcp-iron plastically deformed up to 17.5 GPa and 600 K: experiment and model. *Modelling Simul. Mater. Sci. Eng.* **20**, 024005 (2012).
- Singh, A. K. & Balasingh, C. The lattice strains in a specimen (hexagonal system) compressed nonhydrostatically in an opposed anvil high pressure setup. *J. Appl. Phys.* **75**, 4956–4962 (1994).
- Singh, A. K., Balasingh, C., Mao, H. K., Hemley, R. J. & Shu, J. Analysis of lattice strains measured under nonhydrostatic pressure. *J. Appl. Phys.* **83**, 7567–7575 (1998).
- Bridgman, P. W. Effects of high shearing stress combined with high hydrostatic pressure. *Phys. Rev.* **48**, 825 (1935).
- Wenk, H. R., Matthies, S., Hemley, R. J., Mao, H. K. & Shu, J. The plastic deformation of iron at pressures of the Earth's inner core. *Nature* **405**, 1044–1047 (2000).
- Deb, S. K., Wilding, M., Somayazulu, M. & McMillan, P. F. Pressure-induced amorphization and an amorphous-amorphous transition in densified porous silicon. *Nature* **414**, 528–530 (2001).
- Mao, H. K. et al. Elasticity and rheology of Iron above 220 GPa and the nature of the Earth's inner core. *Nature* **396**, 741–743 (1998).
- Ji, C. et al. Shear-induced phase transition of nanocrystalline hexagonal Boron Nitride to Wurtzitic structure at room temperature and low pressure. *Proc. Natl. Acad. Sci. USA* **109**, 19108–19112 (2012).
- Meade, C. & Jeanloz, R. Effect of a coordination change on the strength of amorphous SiO₂. *Science* **241**, 1072–1074 (1988).
- Gao, Y. et al. Shear driven formation of nano-diamonds at sub-gigapascals and 300 K. *Carbon* **146**, 364–368 (2019).
- Levitas, V. I. High-pressure mechanochemistry: conceptual multi-scale theory and interpretation of experiments. *Phys. Rev. B* **70**, 184118 (2004).
- Barge, N. V. & Boehler, R. Effect of non-hydrostaticity on the α - ϵ transition of iron. *High Press. Res.* **6**, 133–140 (2006).
- Downs, R. T. & Singh, A. K. Analysis of deviatoric stress from non-hydrostatic pressure on a single crystal in a diamond anvil cell: the case of monoclinic aegirine, NaFeSi₂O₆. *J. Phys. Chem. Solids* **67**, 1995–2000 (2006).
- Levitas, V. I. High pressure phase transformations revisited. *J. Phys. Condens. Matter* **30**, 163001 (2018).
- Levitas, V. I. & Shvedov, L. K. Low pressure phase transformation from rhombohedral to cubic BN: experiment and theory. *Phys. Rev. B* **65**, 104109 (2002).

28. Blank, V. D. & Estrin, E. I. Phase transitions in solids under high pressure (New York, CRC Press, 2014).
29. Levitas, V. I. Resolving puzzles of the phase-transformation-based mechanism of the deep-focus earthquake. *Nat. Commun.* **13**, 6291 (2022).
30. Steele, B. A., Goldman, N., Kuo, I. F. W. & Kroonblawd, M. P. Mechanochemical synthesis of glycine oligomers in a virtual rotational Diamond anvil cell. *Chem. Sci.* **11**, 7760–7771 (2020).
31. Stolar, T. et al. Mechanochemical prebiotic peptide bond formation. *Angew. Chem. Int. Ed.* **60**, 12727–12731 (2021).
32. Meade, C. & Jeanloz, R. The strength of mantle silicates at high-pressures and room-temperature - implications for the viscosity of the mantle. *Nature* **348**, 533–535 (1990).
33. Moss, W. C., Hallquist, J. O., Reichlin, R., Goettel, K. A. & Martin, S. Finite-element analysis of the diamond anvil cell - achieving 4.6 Mbar. *Appl. Phys. Lett.* **48**, 1258–1260 (1986).
34. Levitas, V. I. Large deformation of materials with complex rheological properties at normal and high pressure (Nova Science Publishers, New York, 1996).
35. Levitas, V. I., Kamrani, M. & Feng, B. Tensorial stress-strain fields and large elastoplasticity as well as friction in diamond anvil cell up to 400 GPa. *NPJ Comput. Mater.* **5**, 94 (2019).
36. Merkel, S., Hemley, R. J. & Mao, H. K. Finite-element modeling of diamond deformation at multimegabar pressures. *Appl. Phys. Lett.* **74**, 656–658 (1999).
37. Pandey, K. K. & Levitas, V. I. Displacement field measurements in traditional and rotational diamond anvil cells. *J. Appl. Phys.* **129**, 115901 (2021).
38. Feng, B. & Levitas, V. I. Coupled elastoplasticity and plastic strain-induced phase transformation under high pressure and large strains: Formulation and application to BN sample compressed in a diamond anvil cell. *Int. J. Plast.* **96**, 156–181 (2017).
39. Feng, B. & Levitas, V. I. Pressure self-focusing effect and novel methods for increasing the maximum pressure in traditional and rotational diamond anvil cells. *Sci. Rep.* **7**, 45461 (2017).
40. Levitas, V. I. High-pressure phase transformations under severe plastic deformation by torsion in rotational anvils. *Mater. Trans.* **60**, 1294–1301 (2019).
41. Ma, Y., Selvi, E., Levitas, V. I. & Hashemi, J. Effect of shear strain on the α - ϵ phase transition of Iron: a new approach in the rotational diamond anvil cell. *J. Phys. Condens. Matter* **18**, S1075 (2006).
42. Errandonea, D., Meng, Y., Somayazulu, M. & Häusermann, D. Pressure-induced $\alpha \rightarrow \omega$ transition in titanium metal: a systematic study of the effects of uniaxial stress. *Phys. B: Condens. Matter* **355**, 116–125 (2005).
43. Levitas, V. I. Recent in situ experimental and theoretical advances in severe plastic deformations, strain-induced phase transformations, and microstructure evolution under high pressure. *Mater. Trans.* 10.2320/matertrans.MT-MF2022055 (2023).
44. Edalati, K. et al. Nanomaterials by severe plastic deformation: review of historical developments and recent advances. *Mater. Res. Lett.* **10**, 163–256 (2022).
45. Patten, J. A., Cherukuri, H. & Yan, J. Ductile-regime machining of semiconductors and ceramics. *In: High-Pressure Surface Science and Engineering*, 543–632 (CRC Press, 2019).
46. Hsieh, S. et al. Imaging stress and magnetism at high pressures using a nanoscale quantum sensor. *Science* **366**, 1349–1354 (2019).
47. Lin, F., Levitas, V., Pandey, K., Yesudhas, S. & Park, C. Rough diamond anvils: steady microstructure, yield surface, and transformation kinetics in Zr. Preprint at <https://doi.org/10.48550/arXiv.2208.08022> (2022).
48. Zhao, Y. & Zhang, J. Enhancement of yield strength in Zirconium metal through high-pressure induced structural phase transition. *Appl. Phys. Lett.* **91**, 201907 (2007).
49. Zhilyaev, A., Gálvez, F., Sharafutdinov, A. & Pérez-Prado, M. Influence of the high-pressure torsion die geometry on the allotropic phase transformations in pure Zr. *Mat. Sci. Eng. A* **527**, 3918–3928 (2010).
50. Hammersley, A. Fit2d: an introduction and overview, in ESRF Internal Report, ESRF97HA02T (Institute of Physics, Bristol, 1997).
51. Hammersley, A., Svensson, S., Hanfland, M., Fitch, A. & Häusermann, D. Two-dimensional detector software: from real detector to idealised image or two-theta scan. *High Press. Res.* **14**, 235–248 (1996).
52. Rietveld, H. A profile refinement method for nuclear and magnetic structures. *J. Appl. Cryst.* **2**, 65–71 (1969).
53. Young, R. The Rietveld Method, (International Union of Crystallography, Oxford University Press, 1993).
54. Toby, B. & Von Dreele, R. GSAS-II: the genesis of a modern open-source all-purpose crystallography software package. *J. Appl. Cryst.* **46**, 544–549 (2013).
55. Ferrari, M. & Lutterotti, L. Method for the simultaneous determination of anisotropic residual stresses and texture by X-ray diffraction. *J. Appl. Phys.* **76**, 7246–7255 (1994).
56. Lutterotti, L. Total pattern fitting for the combined size-strain-stress-texture determination in thin film diffraction. *Nucl. Instrum. Methods Phys. Res. B* **268**, 334–340 (2010).

Acknowledgements

Support from NSF (CMMI-1943710, DMR-2246991, and XSEDE MSS170015), and Iowa State University (Vance Coffman Faculty Chair Professorship and Murray Harpole Chair in Engineering) is greatly appreciated.

Author contributions

V.I.L. conceived the study, supervised the project, developed theoretical models, and secured funding. A.D. performed the simulations. A.D. and V.I.L. prepared the initial manuscript. K.K.P. performed experiments and collected and postprocessed data. All authors contributed to discussions of the data and to the writing of the manuscript.

Competing interests

The authors declare no competing interests.

Additional information

Supplementary information The online version contains supplementary material available at <https://doi.org/10.1038/s41467-023-41680-1>.

Correspondence and requests for materials should be addressed to Valery I. Levitas or Achyut Dhar.

Peer review information *Nature Communications* thanks the anonymous reviewers for their contribution to the peer review of this work. A peer review file is available.

Reprints and permissions information is available at <http://www.nature.com/reprints>

Publisher's note Springer Nature remains neutral with regard to jurisdictional claims in published maps and institutional affiliations.

Open Access This article is licensed under a Creative Commons Attribution 4.0 International License, which permits use, sharing, adaptation, distribution and reproduction in any medium or format, as long as you give appropriate credit to the original author(s) and the source, provide a link to the Creative Commons licence, and indicate if changes were made. The images or other third party material in this article are included in the article's Creative Commons licence, unless indicated otherwise in a credit line to the material. If material is not included in the article's Creative Commons licence and your intended use is not permitted by statutory regulation or exceeds the permitted use, you will need to obtain permission directly from the copyright holder. To view a copy of this licence, visit <http://creativecommons.org/licenses/by/4.0/>.

© The Author(s) 2023

Supplementary Information

Tensorial stress-plastic strain fields in α - ω Zr mixture, transformation kinetics, and friction in diamond anvil cell

Valery I. Levitas^{1,2,3*}, Achyut Dhar^{*1}, K.K. Pandey⁴

¹ Department of Aerospace Engineering, Iowa State University, Ames, IA 50011, USA

² Department of Mechanical Engineering, Iowa State University, Ames, IA 50011, USA

³ Ames National Laboratory, Division of Materials Science and Engineering, Ames, IA 50011, USA

⁴ High Pressure and Synchrotron Radiation Physics Division, Bhabha Atomic Research Centre, Bombay, Mumbai-400085, India

This PDF file includes:

1. Coupled experimental-analytical-computational approaches for finding stress and plastic strain tensor fields and friction rules in a sample compressed in DAC
2. Coupled Experimental-Analytical (CEA) approach
3. The reasons for the difference between stresses and elastic strains from Rietveld refinement and CEA approach
4. FEM simulations
5. Friction stress and rules for α - and ω -Zr and their mixture
6. Pressure-dependence of the yield strengths of α - and ω -Zr
7. Equation of state under hydrostatic loading

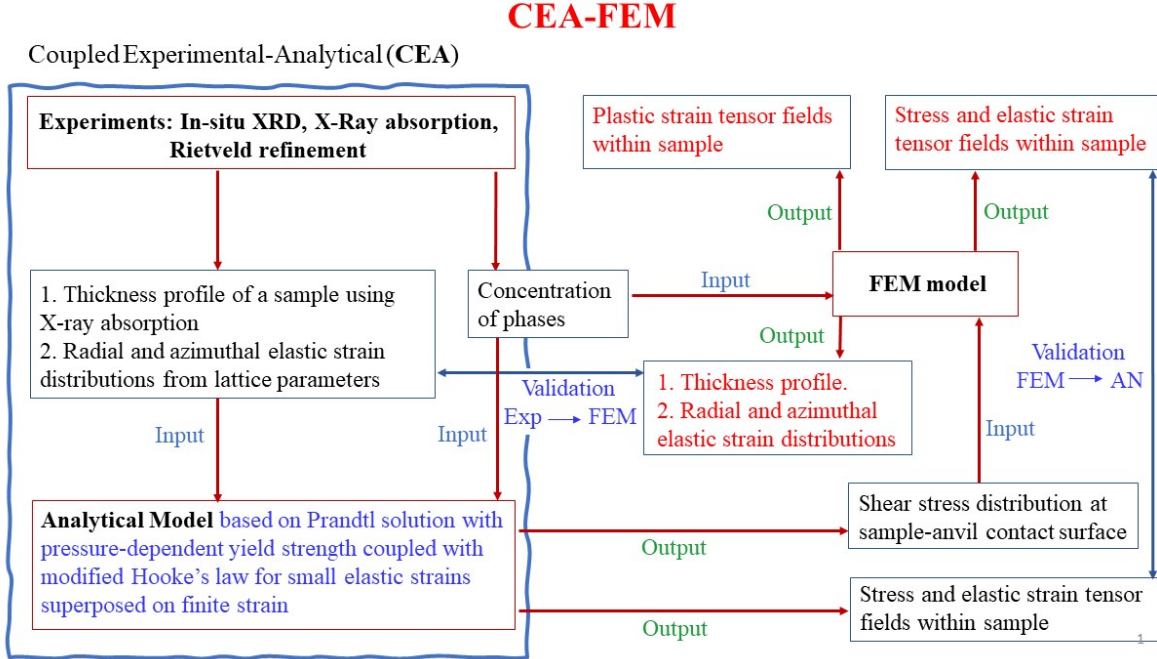
Supplementary Figures

Supplementary References

Supplementary Notes

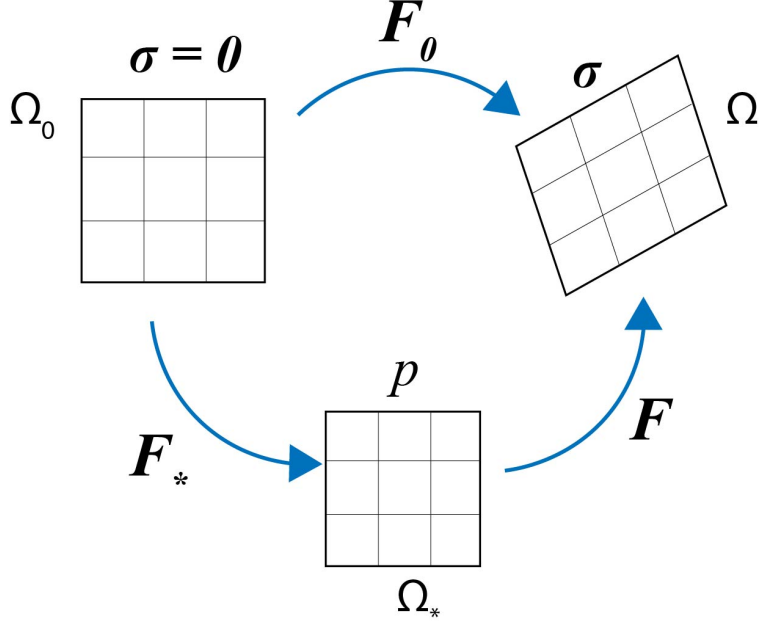
1 Coupled experimental-analytical-computational approaches for finding stress and plastic strain tensor fields and friction rules in a sample compressed in DAC

The flowchart of the interaction between different methods is presented in Supplementary Fig. 1.



Supplementary Fig. 1: **The flowchart of the interaction between experimental, analytical, and FE methods.**

Experimental methods based on in-situ X-ray diffraction and absorption allow us to find the radial $\bar{E}_{0,rr}$ and the azimuthal $\bar{E}_{0,\theta\theta}$ strain distributions in α -Zr and ω -Zr phases, and concentration of ω phase $c(r)$ (all averaged over the sample thickness), as well as sample thickness profile $h(r)$. These distributions are the input data for our analytical model, which allows us to determine the distribution of the contact friction stress at the sample-anvil surface and 2D fields of all components of the stress and elastic strain tensors in each phase and mixture. The friction stress distribution is utilized as the boundary condition in our FEM problem formulation; the evolution of the concentration of ω phase $c(r)$ is introduced homogeneously along the z -coordinate in our FEM problem formulation. FEM solution delivers all components of stress, elastic, and plastic strain tensors and the sample thickness profile. FEM-based radial $\bar{E}_{0,rr}$ and azimuthal $\bar{E}_{0,\theta\theta}$ strain distributions and the sample thickness profile are compared with experiments to validate FEM modeling, and, consequently, the entire procedure and all fields. All components of the stress and elastic strain tensors in the mixture from the analytical solution are compared with the FEM solution to validate the analytical model.



Supplementary Fig. 2: The stress-free configuration Ω_0 , the deformed (current) configuration Ω under the Cauchy stress σ , and an arbitrary intermediate configuration Ω_* with Cauchy stress σ_* . Multiplicative decomposition of the deformation gradient $F_0 = F \cdot F_*$ is valid.

2 Coupled Experimental-Analytical (CEA) approach

To obtain the analytical solution for stress and elastic strain fields in a sample compressed in DAC, we will make a number of strong and counterintuitive assumptions. Surprisingly, the final analytical solution is in good agreement with the much more precise FEM solution (Fig. 1 and Fig. 2 in the main text), which justifies the admissibility of our assumptions.

2.1 Modified Hooke's law under pressure [2]

Let the total deformation gradient from the undeformed stress-free reference configuration to the current deformed configuration $F_0 = F \cdot F_*$ is decomposed multiplicatively into deformation gradient F_* corresponding to hydrostatically loaded with pressure p intermediate configuration and the deformation gradient F that describes small strains from the intermediate to current configuration (Supplementary Fig. 2). Then the modified Hooke's law is:

$$\boldsymbol{\sigma} = -p(\mathbf{F}_*)\mathbf{I} + \mathbf{B}(p) : \tilde{\boldsymbol{\varepsilon}}; \quad \tilde{\boldsymbol{\varepsilon}} = (\mathbf{F} - \mathbf{I})_s; \quad (1)$$

$$\sigma_{ij} = -p(F_{*mn})\delta_{ij} + B_{ijkl}(p)\tilde{\varepsilon}_{lk}; \quad \tilde{\varepsilon}_{lk} = (F_{lk} - \delta_{lk})_s, \quad (2)$$

where $\boldsymbol{\sigma}$ is the Cauchy (true) stress, pressure $p = -(\sigma_{11} + \sigma_{22} + \sigma_{33})/3$, \mathbf{I} is the identity tensor, \mathbf{B} is the pressure-dependent elastic moduli tensor that connects Jaumann derivative of the Cauchy stress and the strain-rate (often called the Wallace moduli). Deformation

gradient $\mathbf{F}_*(p)$ is measured under hydrostatic DAC experiments and for hexagonal crystals considered here it is:

$$\mathbf{F}_*(p) = \begin{bmatrix} F_{*11} & 0 & 0 \\ 0 & F_{*22} & 0 \\ 0 & 0 & F_{*33} \end{bmatrix}, \quad (3)$$

where $F_{*11}(p) = F_{*22}(p) = \frac{a_*}{a_0}$ and $F_{*33}(p) = \frac{c_*}{c_0}$, a_0, c_0 and a_*, c_* are the lattice parameters in the reference and pressurized configurations, respectively. It is important to note that here \mathbf{F}_* is written in the local crystal coordinate system, i.e. F_{*11} and F_{*22} are in the basal slip plane, and F_{*33} is normal to the basal slip plane.

The results of our hydrostatic experiments can be approximated as

$$F_{*11}^\alpha(p) = 1.00 - 0.00372p + 0.00006p^2; \quad (4)$$

$$F_{*33}^\alpha(p) = 1.0 - 0.00333p + 0.00006p^2; \quad (5)$$

$$F_{*11}^\omega(p) = 1.00 - 0.00330p + 0.00003p^2, \quad (6)$$

and

$$F_{*33}^\omega(p) = 1.0 - 0.00282p + 0.00002p^2. \quad (7)$$

Approximation for $\alpha - Zr$ is valid up to 10 GPa, and for $\omega - Zr$ up to 20 GPa.

Since \mathbf{F}_* is diagonal and \mathbf{F} describes small strains, then \mathbf{F}_0 has the form

$$\mathbf{F}_0 = \begin{bmatrix} F_{0,11} & \gamma_1 & 0 \\ \gamma_2 & F_{0,22} & 0 \\ 0 & 0 & F_{0,33} \end{bmatrix}, \quad (8)$$

where generally $\gamma_1 \neq \gamma_2$ because of rotations superposed on the shear strains, and we took into account zero shears for the axisymmetric problem.

We need to express $\tilde{\boldsymbol{\varepsilon}}$, which participates in the Hooke's law (1), with \mathbf{F} and \mathbf{F}_* , which are measured. Since $\tilde{\boldsymbol{\varepsilon}}$ is small, therefore,

$$\tilde{\boldsymbol{\varepsilon}} \approx \mathbf{E} = \mathbf{F}_*^{-1T}(p) \cdot (\mathbf{E}_0 - \mathbf{E}_*(p)) \cdot \mathbf{F}_*^{-1}(p); \quad (9)$$

$$\tilde{\varepsilon}_{lk} \approx E_{lk} = F_{*ik}^{-1}(p) (E_{0,ij} - E_{*ij}(p)) F_{*jl}^{-1}(p), \quad (10)$$

where $\mathbf{E} = 0.5 (\mathbf{F}^T \cdot \mathbf{F} - \mathbf{I})$ is the Lagrangian strain corresponding to \mathbf{F} , $\mathbf{E}_* = 0.5 (\mathbf{F}_*^T \cdot \mathbf{F}_* - \mathbf{I})$ and $\mathbf{E}_0 = 0.5 (\mathbf{F}_0^T \cdot \mathbf{F}_0 - \mathbf{I})$ are the Lagrangian strains corresponding to \mathbf{F}_* and \mathbf{F}_0 . For

\mathbf{F}_0 in Eq. (8), we obtain

$$\mathbf{E}_0 = 0.5 \begin{bmatrix} F_{0,11}^2 - 1 + \gamma_2^2 & F_{0,11}\gamma_1 + F_{0,22}\gamma_2 & 0 \\ F_{0,11}\gamma_1 + F_{0,22}\gamma_2 & F_{0,22}^2 - 1 + \gamma_1^2 & 0 \\ 0 & 0 & F_{0,33}^2 - 1 \end{bmatrix} \simeq 0.5 \begin{bmatrix} F_{0,11}^2 - 1 & \gamma & 0 \\ \gamma & F_{0,22}^2 - 1 & 0 \\ 0 & 0 & F_{0,33}^2 - 1 \end{bmatrix}; \quad \gamma := F_{0,11}\gamma_1 + F_{0,22}\gamma_2, \quad (11)$$

where we neglected small γ_i^2 in comparison with the finite $F_{0,ii}^2 - 1$. Similarly,

$$\mathbf{E}_* = 0.5 \begin{bmatrix} F_{*11}^2 - 1 & 0 & 0 \\ 0 & F_{*22}^2 - 1 & 0 \\ 0 & 0 & F_{*33}^2 - 1 \end{bmatrix}. \quad (12)$$

Then, based on Eq. (9),

$$\tilde{\boldsymbol{\varepsilon}} = 0.5 \begin{bmatrix} \frac{E_{0,11} - E_{*11}}{F_{*11}^2} & \frac{\gamma}{F_{*11}F_{*22}} & 0 \\ \frac{\gamma}{F_{*11}F_{*22}} & \frac{E_{0,22} - E_{*22}}{F_{*22}^2} & 0 \\ 0 & 0 & \frac{E_{0,33} - E_{*33}}{F_{*33}^2} \end{bmatrix} = 0.5 \begin{bmatrix} \frac{F_{0,11}^2}{F_{*11}^2} - 1 & \frac{\gamma}{F_{*11}F_{*22}} & 0 \\ \frac{\gamma}{F_{*11}F_{*22}} & \frac{F_{0,22}^2}{F_{*22}^2} - 1 & 0 \\ 0 & 0 & \frac{F_{0,33}^2}{F_{*33}^2} - 1 \end{bmatrix}. \quad (13)$$

With the obtained structure of $\tilde{\boldsymbol{\varepsilon}}$, the Hooke's law for a hydrostatically pre-stressed hexagonal crystals can be split for normal and shear τ stresses:

$$\begin{bmatrix} \sigma_{11} + p \\ \sigma_{22} + p \\ \sigma_{33} + p \end{bmatrix} = \begin{bmatrix} \hat{\sigma}_{11} \\ \hat{\sigma}_{22} \\ \hat{\sigma}_{33} \end{bmatrix} = \begin{bmatrix} B_{11} & B_{12} & B_{13} \\ B_{12} & B_{22} & B_{23} \\ B_{13} & B_{23} & B_{33} \end{bmatrix} \begin{bmatrix} \tilde{\varepsilon}_{11} \\ \tilde{\varepsilon}_{22} \\ \tilde{\varepsilon}_{33} \end{bmatrix}; \quad \tau = \tau_{13} = 0.5B_{44} \frac{\gamma}{F_{*11}F_{*22}}, \quad (14)$$

where the simplifications due to hexagonal symmetry of B_{ij} ($B_{11} = B_{22}$, $B_{13} = B_{23}$, $B_{44} = B_{55}$, and $B_{66} = 0.5(B_{11} - B_{12})$) were not yet applied. Since XRD does not measure elastic shear strains, equation for shear components will not be used in further derivations. However, after we will find field of the shear stress τ in the sample, we can use the second Eq. (14) to find elastic shear strain γ .

Pressure-dependence of the single crystal elastic moduli B_{ij} was approximated by a quadratic polynomial with parameters given for α -Zr in Table 1 and for the effective elastic moduli B_{ij}^e for ω -Zr in Table 2. They were produced by combining published experimental and first-principle results ([3] for α -Zr and [4] for ω -Zr) and implementing consistency conditions (see [2]) with our hydrostatic experiments; i.e., elastic moduli B_{ij} reproduce generalized equations of state Eqs. (4)-(7). Effective elastic moduli are defined in Eq. (66) with allowing for an actual orientation of a single crystal with respect to the coordinate system and some additional symmetry requirements.

Note that small strain $\tilde{\boldsymbol{\varepsilon}}$ causes change in pressure. We can iteratively update p (and corresponding \mathbf{F}_*) in the intermediate configuration, so that it coincides with the pressure in the current configuration. Then strain $\tilde{\boldsymbol{\varepsilon}}$ will produce deviatoric stress, which is limited

Supplementary Table 1: Elastic constants and their pressure derivatives for α -Zr that meet the consistency conditions.

α -Zr	B_{11}	B_{33}	B_{12}	B_{13}	B_{44}
B_{ij} (GPa)	141.3	159.28	70.97	62.94	32.14
dB_{ij}/dp	2.86	3.04	2.44	2.86	-0.22
d^2B_{ij}/dp^2	0.14	0.176	0.12	0.12	0

Supplementary Table 2: Effective elastic constants and their pressure derivatives for ω -Zr that satisfy the consistency conditions.

ω -Zr	B_{11}^e	B_{33}^e	B_{13}^e
B_{ij}^e (GPa)	169.95	168	72.67
dB_{ij}^e/dp	1.84	2.02	1.47
$d^2B_{ij}^e/dp^2$	0.06	0.076	0.068

by the yield strength. Therefore, strain $\tilde{\epsilon}$ is also limited and is small in comparison with \mathbf{E}_* , which does not have any constraints.

2.2 Approximate analytical solution of axisymmetric problem on compression of a sample

We consider a polycrystalline material compressed by diamond anvils in axisymmetric formulation. We assume that macroscopically material behaves like perfectly plastic and isotropic. Such behavior can be achieved after large-enough preliminary plastic deformation [5, 6].

System of equations and assumptions. The pressure-dependent von Mises yield condition (i.e., Drucker-Prager yield condition) is assumed

$$(\sigma_{11} - \sigma_{22})^2 + (\sigma_{11} - \sigma_{33})^2 + (\sigma_{22} - \sigma_{33})^2 + 6\tau_{13}^2 = 2\sigma_y^2(p) = 6\tau_y^2(p), \quad (15)$$

where σ_{33} , σ_{11} and σ_{22} are the normal stress components along the load (vertical), radial and azimuthal directions, respectively (Supplementary Fig. 3), $\tau = \tau_{13}$ is the shear stress, and σ_y and τ_y are the yield strengths in compression and shear, respectively. Based on experimental results for α - and ω -Zr,

$$\sigma_y = \sqrt{3}\tau_y = \sigma_y^0 + bp, \quad (16)$$

where constants σ_y^0 and b are from Supplementary Fig. 9. Equilibrium equations are

$$\frac{\partial\sigma_{11}}{\partial r} + \frac{\partial\tau_{13}}{\partial z} + \frac{\sigma_{11} - \sigma_{22}}{r} = 0 \quad \text{in radial direction;} \quad (17)$$

$$\frac{\partial\sigma_{33}}{\partial z} + \frac{\partial\tau_{13}}{\partial r} + \frac{\tau_{13}}{r} = 0 \quad \text{in axial direction.} \quad (18)$$

The following assumptions are accepted:

1. As it approximately follows from DAC experiments and FEM simulations for polycrystals (based on the phenomenological flow theory of plasticity)

$$\sigma_{11} = \sigma_{22}. \quad (19)$$

Then the yield condition (15) simplifies to

$$(\sigma_{11} - \sigma_{33})^2 + 3\tau_{13}^2 = \sigma_y^2(p) = 3\tau_y^2(p). \quad (20)$$

2. Stress σ_{33} is independent of z . This does not mean that

$$\frac{\partial \tau_{13}}{\partial r} + \frac{\tau_{13}}{r} = 0 \quad \rightarrow \quad \tau_{13} = \tau_0(z) \frac{r_0}{r}, \quad (21)$$

r_0 and $\tau_0(z)$ being arbitrary constants, because for material with pressure-independent yield strength, $\tau_0(z)$ at the contact surface $z = h$ ($h = h(r)$ is the half of the sample thickness profile determined from the experiments) may be equal to the constant τ_y for all r at the contact surface. Approximate independence of σ_{33} of z means that two other terms in Eq. (18) make small contribution to σ_{33} .

Solution. A slightly modified Prandtl's solution (which was for a plane strain problem [7]) for stresses that satisfies equilibrium equations, plasticity condition, and the above assumptions is:

$$\frac{\sigma_{33}}{\tau_y} = \frac{\sigma_{33}^s}{\tau_y} + \frac{mr}{h}; \quad (22)$$

$$\frac{\tau_{13}}{\tau_y} = \frac{mz}{h}; \quad (23)$$

$$\frac{\sigma_{11}}{\tau_y} = \frac{\sigma_{33}^s}{\tau_y} + \frac{mr}{h} + \sqrt{3} \sqrt{1 - \left(\frac{mz}{h}\right)^2} = \frac{\sigma_{33}}{\tau_y} + \sqrt{3} \sqrt{1 - \left(\frac{mz}{h}\right)^2}; \quad (24)$$

$$p = -(2\sigma_{11} + \sigma_{33})/3, \quad (25)$$

where σ_{33}^s is the stress σ_{33} at the symmetry axis $r = 0$ and parameter $0 \leq m(r) \leq 1$ is defined by the value of shear stress τ_c at the contact surface, $\tau_c = m\tau_y$; $m(0) = 0$ at the symmetry axis. The difference with the Prandtl's solution is in multiplier $\sqrt{3}$ instead of 2 in Eq. (24) for σ_{11} . The reason is that we use von Mises condition and $\sigma_{11} = \sigma_{22}$, which results in Eq. (20), while in the Prandtl's solution the Tresca condition along with plane strain assumption lead to the yield condition $(\sigma_{11} - \sigma_{33})^2 + 4\tau_{13}^2 = \sigma_y^2 = 4\tau_y^2$.

Averaging over the sample thickness. For averaging all stresses over the sample thickness, to get transparent analytical results, we have to assume that the yield strength τ_y depends

on the pressure averaged over the sample thickness,

$$\bar{p} = \frac{1}{h} \int_0^h p dz, \quad (26)$$

i.e.,

$$\sigma_y = \sqrt{3}\tau_y = \sigma_y^0 + b\bar{p}. \quad (27)$$

Then the stress $\bar{\sigma}_{11}$ averaged over the sample thickness is

$$\bar{\sigma}_{11} = \frac{1}{h} \int_0^h \sigma_{11} dz = \sigma_{33} + (\sigma_y^0 + b\bar{p}) \frac{m\sqrt{1-m^2} + \arcsin(m)}{2m}. \quad (28)$$

Averaged pressure

$$\bar{p} = -\frac{2}{3}\bar{\sigma}_{11} - \frac{1}{3}\sigma_{33} = -\sigma_{33} - \frac{2}{3}(\sigma_y^0 + b\bar{p}) \frac{m\sqrt{1-m^2} + \arcsin(m)}{2m}, \quad (29)$$

where we substituted Eq. (28) for $\bar{\sigma}_{11}$. Resolving this equation for σ_{33} , we obtain

$$\sigma_{33} = -\bar{p} - \frac{2}{3}(\sigma_y^0 + b\bar{p}) \frac{m\sqrt{1-m^2} + \arcsin(m)}{2m}. \quad (30)$$

Substituting σ_{33} from Eq. (30) in Eq. (28) and resolving for $\bar{\sigma}_{11}$, we derive

$$\bar{\sigma}_{11} = -\bar{p} + \frac{1}{3}(\sigma_y^0 + b\bar{p}) \frac{m\sqrt{1-m^2} + \arcsin(m)}{2m}. \quad (31)$$

Thus, if friction stress in terms of m and homogeneous along z axis stress σ_{33} are known, \bar{p} and $\bar{\sigma}_{11}$ can be calculated.

Let us analyze the z -dependent part of normal stress and its averaged value:

$$\frac{\sigma_{11} - \sigma_{33}}{\sqrt{3}\tau_y} = \sqrt{1 - \left(\frac{mz}{h}\right)^2}; \quad \frac{\bar{\sigma}_{11} - \sigma_{33}}{\sqrt{3}\tau_y} = \frac{m\sqrt{1-m^2} + \arcsin(m)}{2m}. \quad (32)$$

Note that the averaged value $\bar{\sigma}_{11} - \bar{\sigma}_{33}$ is much closer to the value of $\sigma_{11} - \sigma_{33}$ at the symmetry plane than at the contact surface. Indeed, at the symmetry plane $(\sigma_{11}(0) - \sigma_{33})/(\sqrt{3}\tau_y) = 1$ for all m ; for example, for $m = 1$, we have at the contact surface $(\sigma_{11}(1) - \sigma_{33})/(\sqrt{3}\tau_y) = 0$, while averaged value is $(\bar{\sigma}_{11} - \sigma_{33})/(\sqrt{3}\tau_y) = 0.79$.

Relation between averaged stresses and stresses at the contact surface and symmetry plane. Our next objective is to find relationship between $\bar{\sigma}_{11}$ and $\sigma_{11}(0)$ and $\sigma_{11}(1)$ to be used for interpretation of experimental results. We will use the following identity

$$\begin{aligned} \bar{\sigma}_{11} &= \sigma_{11}(1)w + \sigma_{11}(0)(1-w); \\ w(m) &= \frac{\bar{\sigma}_{11} - \sigma_{11}(0)}{\sigma_{11}(1) - \sigma_{11}(0)} = \frac{\sqrt{1-m^2} + \arcsin(m)/m - 2}{2(\sqrt{1-m^2} - 1)}, \end{aligned} \quad (33)$$

where $w(m)$ is treated as the weight factor, which varies in a narrow range between $w(1) = 1 - \pi/4 \simeq 0.215$ and $w(0) = 1/3$. Since σ_{33} is independent of z , we have similar equation for pressure:

$$\bar{p} = p(1)w + p(0)(1 - w). \quad (34)$$

2.3 Special stress states

Here we considered two main stress states under plastic deformation.

1. Along the symmetry axis ($r = m = 0$) and at the symmetry plane ($z = 0$), shear stress is zero, and the stress components along the load axis (Supplementary Fig. 3) are defined by Eq. (24):

$$\sigma_{11}^s = \sigma_{33}^s + \sigma_y; \quad \sigma_{11}(0) = \sigma_{22}(0) = \sigma_{33} + \sigma_y, \quad (35)$$

where we took into account that σ_{33} is assumed to be independent of z . Note that compressive normal stresses are negative. Then for pressure one obtains

$$p^s = p(0) = -(\sigma_{33} + 2/3\sigma_y(\bar{p})). \quad (36)$$

2. At sample-diamond contact surface $z/h = 1$, Eq. (24) results in

$$\sigma_{11}(1) = \sigma_{22}(1) = \sigma_{33} + \sigma_y(\bar{p})\sqrt{1 - m^2}. \quad (37)$$

and

$$p(1) = -(\sigma_{33} + 2/3\sigma_y(\bar{p})\sqrt{1 - m^2}). \quad (38)$$

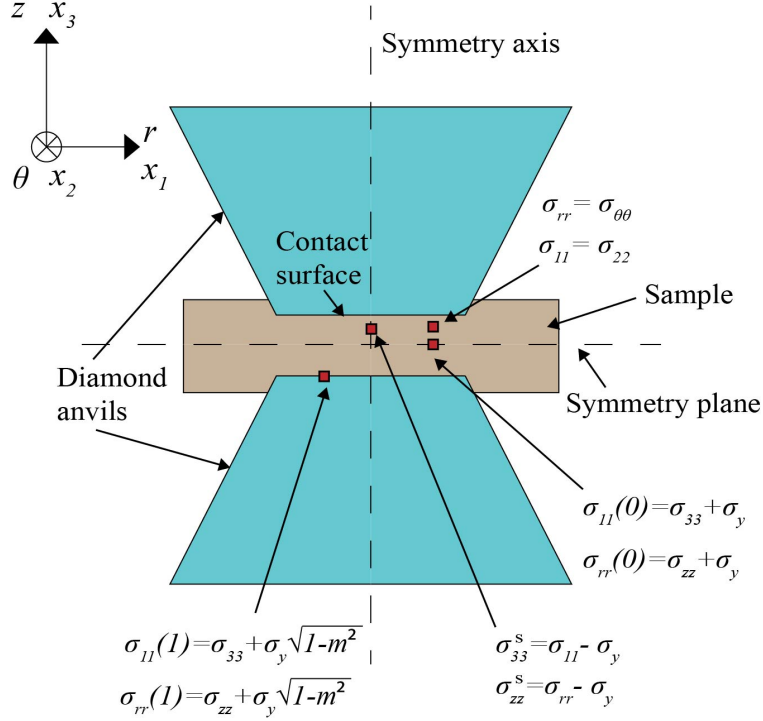
When the friction shear stress reaches the yield strength in shear ($m = 1$), the von Mises yield condition (15) results in

$$\sigma_{11}(1) = \sigma_{22}(1) = \sigma_{33}(1) = -p(1) \quad (39)$$

without the assumption $\sigma_{11} = \sigma_{22}$.

2.4 Application of the modified Hooke's law for α -Zr with c -axis parallel to the loading axis

The modified Prandtl's solution in Section 2.2 allows us to find stress distributions provided that the boundary conditions $m(r)$ for the contact friction and σ_{33}^s are known, but they are not. We have to find a way to utilize experimentally measured fields $\bar{E}_{0,rr}$ and $\bar{E}_{0,\theta\theta}$ to determine $m(r)$ and finalize our analytical solution. Strong observed texture (with c -axis parallel to the loading axis for α -Zr and to the radial direction for ω -Zr) allows us to utilize single crystal elasticity to find stress distributions in a sample using modified Hooke's law at high pressure. Then the Reuss hypothesis that stresses in all single crystals in the representative



Supplementary Fig. 3: **Schematic illustration of stress states at the symmetry plane, symmetry axis, and the contact surface.**

volume and in polycrystalline aggregate are the same, combined with the simplified mechanical equilibrium condition (59) allow us to connect these stresses and stresses determined by the modified Prandtl's solution and determine $m(r)$, and consequently, all stress and elastic strain fields.

The Hooke's law (14) for hexagonal crystal, in a hydrostatically stressed configuration characterized by pressure p , for normal stresses and strains can be presented in the form

$$\begin{bmatrix} \sigma_{11} + p \\ \sigma_{22} + p \\ \sigma_{33} + p \end{bmatrix} = \begin{bmatrix} \hat{\sigma}_{11} \\ \hat{\sigma}_{22} \\ \hat{\sigma}_{33} \end{bmatrix} = \begin{bmatrix} B_{11} & B_{12} & B_{13} \\ B_{12} & B_{11} & B_{13} \\ B_{13} & B_{13} & B_{33} \end{bmatrix} \begin{bmatrix} \tilde{\epsilon}_{11} \\ \tilde{\epsilon}_{22} \\ \tilde{\epsilon}_{33} \end{bmatrix}. \quad (40)$$

We will not use the second equation (14) for shear strains and stresses because shear strains are not measurable with x-rays and cannot be used for connection to the Prandtl's solution. However, after all stresses, including shear stress will be found, this equation can be used to determine the elastic shear strain.

Using our assumption (19) that $\sigma_{11} = \sigma_{22}$ for a polycrystal and by invoking the Reuss hypothesis, $\sigma_{11} = \sigma_{22}$ in the single crystal is obtained. This equality, using Eq. (40), gives

$$\tilde{\epsilon}_{11} = \tilde{\epsilon}_{22} \rightarrow \bar{\tilde{\epsilon}}_{11} = \bar{\tilde{\epsilon}}_{22}. \quad (41)$$

From Eq. (13) and $F_{*11} = F_{*22}$ we obtain $F_{0,11} = F_{0,22}$ and $E_{0,11} = E_{0,22}$. Averaging these equations over a sample thickness leads to the experimental observation that $\bar{F}_{0,11} = \bar{F}_{0,22}$ and $\bar{E}_{0,11} = \bar{E}_{0,22}$.

For $\sigma_{11} = \sigma_{22}$, one obtains from Eq. (40)

$$\begin{aligned}\tilde{\varepsilon}_{11}(z/h) &= \tilde{\varepsilon}_{22}(z/h) = k(B_{33}\hat{\sigma}_{11}(z/h) - B_{13}\hat{\sigma}_{33}); \\ \tilde{\varepsilon}_{33}(z/h) &= k((B_{11} + B_{12})\hat{\sigma}_{33} - 2B_{13}\hat{\sigma}_{11}(z/h)); \quad k = \left((B_{11} + B_{12})B_{33} - 2B_{13}^2\right)^{-1}.\end{aligned}\quad (42)$$

Averaging over the sample thickness. Averaging Eq. (42) over the thickness, we derive

$$\bar{\tilde{\varepsilon}}_{11} = k(B_{33}(\bar{\sigma}_{11} + \bar{p}) - B_{13}(\bar{\sigma}_{33} + \bar{p})); \quad (43)$$

$$\bar{\tilde{\varepsilon}}_{33} = k((B_{11} + B_{22})(\bar{\sigma}_{33} + \bar{p}) - 2B_{13}(\bar{\sigma}_{11} + \bar{p})). \quad (44)$$

Note that elastic moduli \mathbf{B} are considered homogeneous along the thickness direction for simplicity; they are also considered to be functions of averaged through the thickness pressure \bar{p} , i.e., $\mathbf{B} = \mathbf{B}(\bar{p})$, where $\bar{p} = \bar{p}(r)$. To prove for elastic strains relationship similar to Eq. (33) for stresses, let us derive an alternative expression for $\bar{\varepsilon}_{11}$. It follows from Eq. (42)

$$\tilde{\varepsilon}_{11}(0) = k(B_{33}\hat{\sigma}_{11}(0) - B_{13}\hat{\sigma}_{33}(0)) = k(B_{33}(\sigma_{11}(0) + p(0)) - B_{13}(\sigma_{33} + p(0))); \quad (45)$$

$$\tilde{\varepsilon}_{11}(1) = k(B_{33}(\sigma_{11}(1) + p(1)) - B_{13}(\sigma_{33} + p(1))). \quad (46)$$

We remind that the arguments 0 and 1 designate points at the symmetry plane and the contact surface, respectively. Multiplying Eq. (45) by $1 - w$ and Eq. (46) by w and adding them, we obtain

$$(1 - w)\tilde{\varepsilon}_{11}(0) + w\tilde{\varepsilon}_{11}(1) = k[B_{33}((1 - w)\sigma_{11}(0) + w\sigma_{11}(1)) + B_{33}((1 - w)p(0) + wp(1)) - B_{13}((1 - w)\sigma_{33} + w\sigma_{33} + (1 - w)p(0) + wp(1))]. \quad (47)$$

Using Eq. (34) in Eq. (47), we obtain

$$(1 - w)\tilde{\varepsilon}_{11}(0) + w\tilde{\varepsilon}_{11}(1) = k[B_{33}(\bar{\sigma}_{11} + \bar{p}) - B_{13}(\sigma_{33} + \bar{p})], \quad (48)$$

where the first equation Eq. (33) was utilized. Comparison of Eq. (48) and Eq. (43) leads to important conclusion that the averaged small imposed strains,

$$\bar{\tilde{\varepsilon}}_{11} = \bar{\tilde{\varepsilon}}_{22} = (1 - w)\tilde{\varepsilon}_{11}(0) + w\tilde{\varepsilon}_{11}(1), \quad (49)$$

have similar expressions as the averaged stress $\bar{\sigma}_{11}$ in Eq. (33). This result will be utilized for interpretation of experimental measurements of $\bar{\varepsilon}_{11}$. Similarly, for $\bar{\tilde{\varepsilon}}_{33}$

$$\bar{\tilde{\varepsilon}}_{33} = (1 - w)\tilde{\varepsilon}_{33}(0) + w\tilde{\varepsilon}_{33}(1). \quad (50)$$

At the symmetry plane, using $\tilde{\varepsilon}_{11}(0) = \tilde{\varepsilon}_{22}(0)$, $\sigma_{11}(0) = \sigma_{22}(0)$ and Eq. (35) in Eq. (40), we derive

$$\begin{bmatrix} \sigma_{33} + \sigma_y(\bar{p}) + p(0) \\ \sigma_{33} + \sigma_y(\bar{p}) + p(0) \\ \sigma_{33} + p(0) \end{bmatrix} = \begin{bmatrix} B_{11} & B_{12} & B_{13} \\ B_{12} & B_{11} & B_{13} \\ B_{13} & B_{13} & B_{33} \end{bmatrix} \begin{bmatrix} \tilde{\varepsilon}_{11}(0) \\ \tilde{\varepsilon}_{11}(0) \\ \tilde{\varepsilon}_{33}(0) \end{bmatrix}. \quad (51)$$

At the sample-anvil contact surface, using Eqs. (37), we obtain from Eqs. (40)

$$\begin{bmatrix} \sigma_{33} + \sigma_y(\bar{p})\sqrt{1-m^2} + p(1) \\ \sigma_{33} + \sigma_y(\bar{p})\sqrt{1-m^2} + p(1) \\ \sigma_{33} + p(1) \end{bmatrix} = \begin{bmatrix} B_{11} & B_{12} & B_{13} \\ B_{12} & B_{11} & B_{13} \\ B_{13} & B_{13} & B_{33} \end{bmatrix} \begin{bmatrix} \tilde{\varepsilon}_{11}(1) \\ \tilde{\varepsilon}_{11}(1) \\ \tilde{\varepsilon}_{33}(1) \end{bmatrix}. \quad (52)$$

In order to utilize averaged over the thickness elastic strains $\bar{\varepsilon}_{11} = \bar{\varepsilon}_{22}$ (which are related to $\bar{E}_{0,11} = \bar{E}_{0,22}$ and $\bar{F}_{*11} = \bar{F}_{*22}$ measured in experiments through Eq. (10)), let us multiply Eq. (51) by $1-w$, Eq. (52) by w , and combine them:

$$\begin{bmatrix} B_{11} & B_{12} & B_{13} \\ B_{12} & B_{11} & B_{13} \\ B_{13} & B_{13} & B_{33} \end{bmatrix} \begin{bmatrix} \bar{\varepsilon}_{11} \\ \bar{\varepsilon}_{11} \\ \bar{\varepsilon}_{33} \end{bmatrix} = \begin{bmatrix} \sigma_{33} + (1-w)\sigma_y(\bar{p}) + w\sigma_y(\bar{p})\sqrt{1-m^2} + (1-w)p(0) + wp(1) \\ \sigma_{33} + (1-w)\sigma_y(\bar{p}) + w\sigma_y(\bar{p})\sqrt{1-m^2} + (1-w)p(0) + wp(1) \\ \sigma_{33} + (1-w)p(0) + wp(1) \end{bmatrix} \\ = \begin{bmatrix} \sigma_{33} + (1-w)\sigma_y(\bar{p}) + w\sigma_y(\bar{p})\sqrt{1-m^2} + \bar{p} \\ \sigma_{33} + (1-w)\sigma_y(\bar{p}) + w\sigma_y(\bar{p})\sqrt{1-m^2} + \bar{p} \\ \sigma_{33} + \bar{p} \end{bmatrix}. \quad (53)$$

In obtaining Eq. (53), Eqs. (34), (49) and (50) were used. The advantage of Eq. (53) is that it includes $\bar{\varepsilon}_{11}$, which will allow us to express all stresses and strains in terms of $\bar{\varepsilon}_{11}$. Inversion of Eqs. (53) gives:

$$\bar{\varepsilon}_{33} = k(B_{11} + B_{12} - 2B_{13})(\sigma_{33} + \bar{p}) - 2kB_{13} \left[(1-w)\sigma_y(\bar{p}) + w\sigma_y(\bar{p})\sqrt{1-m^2} \right]. \quad (54)$$

Also, the third Eq. (53) is

$$\sigma_{33} + \bar{p} = 2B_{13}\bar{\varepsilon}_{11} + B_{33}\bar{\varepsilon}_{33}. \quad (55)$$

Substituting Eq. (55) in Eq. (54) and solving for $\bar{\varepsilon}_{33}$, one finds

$$\bar{\varepsilon}_{33} = (B_{33} - B_{13})^{-1} \left[(B_{11} + B_{12} - 2B_{13})\bar{\varepsilon}_{11} - (1-w)\sigma_y(\bar{p}) - w\sigma_y(\bar{p})\sqrt{1-m^2} \right]. \quad (56)$$

Placing Eq. (56) in Eq. (55), we obtain expression for $\sigma_{33} + \bar{p}$:

$$\sigma_{33} + \bar{p} = (B_{13} - B_{33})^{-1} \left[(2B_{13}^2 - B_{11}B_{33} - B_{12}B_{33})\bar{\varepsilon}_{11} + B_{33}\sigma_y(\bar{p}) \left(1 - w + w\sqrt{1-m^2} \right) \right]. \quad (57)$$

Next, we substitute $\sigma_{33} + \bar{p}$ from Eq. (30) in Eq. (57) and obtain nonlinear equation for \bar{p} (if we assume m to be known):

$$\begin{aligned} & (B_{13} - B_{33})^{-1} \left[(2B_{13}^2 - B_{11}B_{33} - B_{12}B_{33})\bar{\varepsilon}_{11} + B_{33}\sigma_y(\bar{p}) \left(1 - w + w\sqrt{1-m^2} \right) \right] \\ & = -\frac{2}{3}(\sigma_y^0 + b\bar{p}) \frac{m\sqrt{1-m^2} + \arcsin(m)}{2m}. \end{aligned} \quad (58)$$

Note that B_{ij} are quadratic functions of pressure, and due to nonlinearity of Eq. (58) in B_{ij} , it is strongly nonlinear in \bar{p} and cannot be solved analytically. After numerical solution

of Eq. (58) for \bar{p} , Eq. (30) gives numerical value of σ_{33} . Note that since experimentally determined strains $\bar{\varepsilon}_{11} = \bar{\varepsilon}_{22}$ are functions of the radius r , Eq. (57) and solution to Eq. (58) also reproduce the radial dependence of σ_{33} and \bar{p} . Then Eqs. (23), (24), and (25) can be used to reproduce z -dependence of the shear stress τ_{13} , normal stresses $\sigma_{11} = \sigma_{22}$, and pressure p . Elastic strains can be found after substituting stresses in Eqs. (42). The next step is to derive the additional equation for m to be combined with Eq. (58).

2.5 Evaluation of friction stress utilizing pressure gradient method

The friction stress τ_c is defined by the simplified mechanical equilibrium equation [5]

$$\frac{d\bar{\sigma}_{11}}{dr} = \frac{\tau_c}{h(r)} = \frac{m(r)\tau_y(\bar{p})}{h(r)}. \quad (59)$$

For solution, we approximated this differential equation with the finite difference equation, using midpoint algorithm, e.g.,

$$\frac{\bar{\sigma}_{11,i+1} - \bar{\sigma}_{11,i-1}}{2\Delta r} = \frac{m_i(\sigma_y^0 + b\bar{p}_i)}{\sqrt{3}h_i}, \quad (60)$$

where subscript i designates value of the function at point r_i . This equation is supplemented with Eqs. (31) and (58) for each radial point r_i :

$$\bar{\sigma}_{11} = -\bar{p} + \frac{1}{3}(\sigma_y^0 + b\bar{p}) \frac{m\sqrt{1-m^2} + \arcsin(m)}{2m}. \quad (61)$$

$$\begin{aligned} & (B_{13} - B_{33})^{-1} \left[(2B_{13}^2 - B_{11}B_{33} - B_{12}B_{33})\bar{\varepsilon}_{11} + B_{33}\sigma_y(\bar{p}) \left(1 - w + w\sqrt{1-m^2} \right) \right] \\ & = -\frac{2}{3}(\sigma_y^0 + b\bar{p}) \frac{m\sqrt{1-m^2} + \arcsin(m)}{2m}. \end{aligned} \quad (62)$$

Eqs. (60)-(62) represent system of 3N nonlinear algebraic/trigonometric equations for 3 unknowns m , \bar{p} , and $\bar{\sigma}_{11}$ in each of N points along the radial direction r , which we solved numerically. Since for $\bar{\sigma}_{11}$ we have explicit expression, which in practice is substituted in Eq. (60), we have 2N nonlinear algebraic/trigonometric equations for 2 unknowns m and \bar{p} in each of N points. Then Eqs. (23), (24), and (25) can be used to reproduce z -dependence of the shear stress τ_{13} , normal stresses $\sigma_{11} = \sigma_{22}$, and pressure p . Elastic strains can be found after substituting stresses in Eqs. (42).

We can pass to FEM simulations, as one of the boundary conditions, either obtained contact shear stress $\tau_c(r)$ or coefficient $m(r)$. In the latter case, it is more precise to redefine m based on the local pressure $p(1)$, i.e., from $\tau_c(r) = m(r)\tau_y(\bar{p}) = m'(r)\tau_y[p(1)]$ and use in FEM simulations m' , because in FEM τ_y at the contact surface depends on $p(1)$. Pressure $p(1)$ can be obtained from Eq. (38), in which σ_{33} is substituted with the expression (30):

$$p(1) = \bar{p} - \frac{1}{3}\sigma_y(\bar{p}) \frac{m\sqrt{1-m^2} - \arcsin(m)}{m}. \quad (63)$$

2.6 Application of the Hooke's law for ω -Zr with c -axis parallel to the radial direction

The modified Hooke's law for hexagonal crystal for normal stresses and strains, when c -axis is parallel to the radial direction 1 can be presented in the form

$$\begin{bmatrix} \sigma_{11} + p \\ \sigma_{22} + p \\ \sigma_{33} + p \end{bmatrix} = \begin{bmatrix} \hat{\sigma}_{11} \\ \hat{\sigma}_{22} \\ \hat{\sigma}_{33} \end{bmatrix} = \begin{bmatrix} B_{33} & B_{13} & B_{13} \\ B_{13} & B_{11} & B_{12} \\ B_{13} & B_{12} & B_{11} \end{bmatrix} \begin{bmatrix} \tilde{\varepsilon}_{11} \\ \tilde{\varepsilon}_{22} \\ \tilde{\varepsilon}_{33} \end{bmatrix}. \quad (64)$$

Our assumption (19) $\sigma_{11} = \sigma_{22}$ for a polycrystal along with the Reuss hypothesis leads to $\sigma_{11} = \sigma_{22}$ for the single crystal. The problem is that this equality substituted in Eq. (64) does not lead to $\tilde{\varepsilon}_{11} = \tilde{\varepsilon}_{22}$ and hence, violates the experimental observation that $\bar{E}_{0,11} = \bar{E}_{0,22}$. That is we need to modify the elastic moduli tensor \mathbf{B} for consistency with experiments.

The simplest way to satisfy $\sigma_{11} = \sigma_{22}$ for polycrystal is to assume that for $\tilde{\varepsilon}_{11} = \tilde{\varepsilon}_{22}$ stresses σ_{11}^p and σ_{22}^p for polycrystal are defined as

$$\sigma_{11}^p = \sigma_{22}^p = 0.5(\sigma_{11} + \sigma_{22}) \quad for \quad \tilde{\varepsilon}_{11} = \tilde{\varepsilon}_{22}. \quad (65)$$

This can be imposed by changing the elastic moduli matrix in Eq. (64) with an "effective" elastic modular matrix

$$\begin{bmatrix} \sigma_{11} + p \\ \sigma_{22} + p \\ \sigma_{33} + p \end{bmatrix} = \begin{bmatrix} \hat{\sigma}_{11} \\ \hat{\sigma}_{22} \\ \hat{\sigma}_{33} \end{bmatrix} = \begin{bmatrix} B_{11}^e & B_{12}^e & B_{13}^e \\ B_{12}^e & B_{11}^e & B_{13}^e \\ B_{13}^e & B_{13}^e & B_{33}^e \end{bmatrix} \begin{bmatrix} \tilde{\varepsilon}_{11} \\ \tilde{\varepsilon}_{22} \\ \tilde{\varepsilon}_{33} \end{bmatrix} = \begin{bmatrix} 0.5(B_{11} + B_{33}) & B_{13} & 0.5(B_{12} + B_{13}) \\ B_{13} & 0.5(B_{11} + B_{33}) & 0.5(B_{12} + B_{13}) \\ 0.5(B_{12} + B_{13}) & 0.5(B_{12} + B_{13}) & B_{11} \end{bmatrix} \begin{bmatrix} \tilde{\varepsilon}_{11} \\ \tilde{\varepsilon}_{22} \\ \tilde{\varepsilon}_{33} \end{bmatrix}. \quad (66)$$

Thus, we substitute elastic constants in positions 11 and 22 in matrix (64) (i.e., B_{33} and B_{11}) with their average $0.5(B_{11} + B_{33})$, and elastic constants in positions 13 and 23 in matrix (64) (i.e., B_{13} and B_{12}) with their average $0.5(B_{12} + B_{13})$, keeping symmetry of the elasticity matrix. Matrix (66) has 4 independent elastic constants, like matrix (64). However, with such a procedure, we violated equality of elastic moduli in positions 12 and 13 in Eq. (64). To restore this equality (symmetry), we accept

$$\begin{bmatrix} \sigma_{11} + p \\ \sigma_{22} + p \\ \sigma_{33} + p \end{bmatrix} = \begin{bmatrix} B_{11}^e & B_{13}^e & B_{13}^e \\ B_{13}^e & B_{11}^e & B_{13}^e \\ B_{13}^e & B_{13}^e & B_{33}^e \end{bmatrix} \begin{bmatrix} \tilde{\varepsilon}_{11} \\ \tilde{\varepsilon}_{22} \\ \tilde{\varepsilon}_{33} \end{bmatrix} = \begin{bmatrix} 0.5(B_{11} + B_{33}) & 0.5(B_{12} + B_{13}) & 0.5(B_{12} + B_{13}) \\ 0.5(B_{12} + B_{13}) & 0.5(B_{11} + B_{33}) & 0.5(B_{12} + B_{13}) \\ 0.5(B_{12} + B_{13}) & 0.5(B_{12} + B_{13}) & B_{11} \end{bmatrix} \begin{bmatrix} \tilde{\varepsilon}_{11} \\ \tilde{\varepsilon}_{22} \\ \tilde{\varepsilon}_{33} \end{bmatrix}. \quad (67)$$

Reduction in number of independent elastic moduli for normal strains from 4 to 3 in transition from a single crystal to textured polycrystal is natural. After such a modification of the \mathbf{B} -matrix, all equations (42)-(62) for α -Zr can be applied with adding superscript e to

components B_{ij} and imposing $B_{12} = B_{13}$.

2.7 Generalization for the two-phase mixture

Equations for each phase. Radial distribution of volume fraction of the low- and high-pressure phases, averaged over the sample thickness, c_1 and $c_2 = 1 - c_1 = c$, are determined from the experiment using Rietveld refinement. It is independent of the interpretation of stresses and strains and does not participate in the iterations to determine distribution of the stress and elastic strain tensors. Radial distributions of strain $\bar{E}_{0,11}^1 = \bar{E}_{0,22}^2$ is measured in each phase 1 and 2. The modified Hooke's law and plasticity condition are satisfied for each phase separately. We assume

$$m_1 = m_2 = m \quad (68)$$

and that $\sigma_{11}^k = \sigma_{22}^k$, σ_{33}^k is independent of z , and Eqs. (22) - (24) are valid for stresses in each phase. Then Eqs. (22) - (67) are valid for each phase with the elastic constants and the yield strength of each phase, all in terms of experimentally measured elastic strains $\bar{E}_{0,11}^k = \bar{E}_{0,22}^k$ in each phase. That means that for two-phase material, we have to perform the same procedure and use the same equations for each phase separately and find solution in each phase separately. This does not mean that we completely neglect interaction between phases, because the experimentally measured elastic strains $\bar{E}_{0,11}^k = \bar{E}_{0,22}^k$ in each phase do include such an interaction.

Equations for mixture. Since all fields in each phase are known, here we define averaging rules to determine fields in the mixture. We assume for deformation gradient under hydrostatic pressure \mathbf{F}_* , elastic superposed strains ε_{ii} , and for stresses σ_{ii}

$$\begin{aligned} \mathbf{F}_* &= c_1 \mathbf{F}_*^1 + c_2 \mathbf{F}_*^2; & E_{0,ii} &= c_1 E_{0,ii}^1 + c_2 E_{0,ii}^2; & \gamma &= c_1 \gamma^1 + c_2 \gamma^2; \\ \sigma_{ii} &= c_1 \sigma_{ii}^1 + c_2 \sigma_{ii}^2; & \tau &= c_1 \tau^1 + c_2 \tau^2; & \tilde{\varepsilon}_{ii} &= c_1 \tilde{\varepsilon}_{ii}^1 + c_2 \tilde{\varepsilon}_{ii}^2. \end{aligned} \quad (69)$$

While for stresses the averaging equation is exact, for elastic strain and \mathbf{F}_* they represent strong assumption, because \mathbf{F}_* and $\tilde{\varepsilon}$ are incompatible separately even in the absence of the plastic and transformation strains, because of heterogeneous pressure distribution, and consequently \mathbf{F}_* . For shear stress at the contact surface, in particular,

$$\tau_c = m\tau_y = c_1 \tau_{c1}(\bar{p}_1) + c_2 \tau_{c2}(\bar{p}_2) = m(c_1 \tau_{y1}(\bar{p}_1) + c_2 \tau_{y2}(\bar{p}_2)), \quad (70)$$

where from we obtain the mixture rule for the pressure-dependent yield strength

$$\begin{aligned} \tau_y &= c_1 \tau_{y1}(\bar{p}_1) + c_2 \tau_{y2}(\bar{p}_2); \\ \sigma_y &= \sqrt{3}\tau_y = c_1 \sigma_{y1}(\bar{p}_1) + c_2 \sigma_{y2}(\bar{p}_2) = c_1 \sigma_{y1}^0 + c_2 \sigma_{y2}^0 + c_1 b_1 \bar{p}_1 + c_2 b_2 \bar{p}_2. \end{aligned} \quad (71)$$

2.8 Explicit relationships between $\tilde{\epsilon}$, E and F_*

It follows from Eq. (10) or (13) that

$$\tilde{\epsilon}_{11} = \tilde{\epsilon}_{22} = \frac{E_{0,11} - 0.5 \left((F_{*11}(p))^2 - 1 \right)}{(F_{*11}(p))^2}, \quad (72)$$

where for $\alpha - Zr$ $F_{*11}(p)$ is given by Eq. (4). It is important to note that the $\alpha - Zr$ crystal coordinate system coincides with the global coordinate system and therefore the local $F_{*11}(p)$ coincides with the global in Eq. (72). Averaged over the sample thickness $\bar{\epsilon}_{11}$, which is present in Eq. (56), can be obtained from Eq. (72) as follows:

$$\bar{\epsilon}_{11} = \frac{1}{h} \int_0^h \left(\frac{E_{0,11}}{(F_{*11}(p))^2} + \frac{1}{2} \frac{1}{(F_{*11}(p))^2} - \frac{1}{2} \right) dz \quad (73)$$

Based on Eq. (4), we can approximate in the pressure range of 0 – 10 GPa as $\frac{1}{(F_{*11}(p))^2} = 1 + 0.00668p$. Using this, Eq. (73) can be written as

$$\bar{\epsilon}_{11} = \frac{0.00668}{h} \int_0^h E_{0,11} p dz + \bar{E}_{0,11} + 0.00334\bar{p}. \quad (74)$$

It is impossible to evaluate $\int_0^h E_{0,11} p dz$ in terms of \bar{p} and $\bar{E}_{0,11}$ without knowing the distribution of $E_{0,11}$ and therefore, it is approximated as:

$$\frac{1}{h} \int_0^h E_{0,11} p dz \simeq \bar{E}_{0,11} \bar{p}. \quad (75)$$

Combination of Eqs. (75) and (74) results in

$$\bar{\epsilon}_{11} = 0.00668 \bar{E}_{0,11} \bar{p} + \bar{E}_{0,11} + 0.00334 \bar{p}. \quad (76)$$

As it was already mentioned that the c -axis of ω -Zr crystal is primarily oriented along the global 1 direction and therefore, it is local $F_{*33}(p)$ (rather than the local $F_{*11}(p)$) that coincides with the global 1 direction, unlike for the α -Zr. Also, to enforce $\tilde{\epsilon}_{11} = \tilde{\epsilon}_{22}$, given $\bar{E}_{0,11} = \bar{E}_{0,22}$ from experiments, Eq. (72) transforms for ω -Zr as:

$$\tilde{\epsilon}_{11} = \tilde{\epsilon}_{22} = \frac{E_{0,11} - 0.5 \left((F_{*11}^{ef}(p))^2 - 1 \right)}{(F_{*11}^{ef}(p))^2}, \quad (77)$$

where, $F_{*11}^{ef} = F_{*22}^{ef} = 0.5(F_{*11}^\omega + F_{*33}^\omega)$. $F_{*11}^\omega(p)$ and $F_{*33}^\omega(p)$ given in Eqs. (6) and (7) are written here again for convenience:

$$F_{*11}^\omega(p) = 1.00 - 0.00330p + 0.00003p^2, \quad (78)$$

and

$$F_{*33}^\omega(p) = 1.0 - 0.00282p + 0.00002p^2. \quad (79)$$

Following the same averaging procedure as was done with α -Zr, for a pressure range of 0 – 20 GPa, the approximation for ω -Zr is

$$\frac{1}{\left(F_{*11}^{ef}(p)\right)^2} = 1.0 + 0.0055p \quad (80)$$

resulting in

$$\bar{\varepsilon}_{11} = \bar{\varepsilon}_{22} = 0.0055\bar{E}_{0,11}\bar{p} + \bar{E}_{0,11} + 0.0028\bar{p}. \quad (81)$$

Likewise, from Eq. (10) for direction 3 we have:

$$E_{0,33} = \tilde{\varepsilon}_{33} (F_{*33}(p))^2 + 0.5((F_{*33}(p))^2 - 1). \quad (82)$$

Eq. (82) is not used in further derivations; it just defines the total Lagrangian strain $E_{0,33}$ when $\tilde{\varepsilon}_{33}$ is already found. Since function F_{*33} is given by Eq. (5) for $\alpha - Zr$, it can be approximated by

$$(F_{*33}(p))^2 = 1 - 0.00664p + 0.00013p^2. \quad (83)$$

For the rotated $\omega - Zr$ crystal, the $E_{0,33}$ in the global coordinate system is as follows:

$$E_{0,33} = \tilde{\varepsilon}_{33} \left(F_{*33}^{ef}(p)\right)^2 + 0.5 \left(\left(F_{*33}^{ef}(p)\right)^2 - 1\right), \quad (84)$$

where $F_{*33}^{ef} = F_{*11}^\omega$ and $\left(F_{*33}^{ef}(p)\right)^2 = 1 - 0.0066p + 0.000077p^2$ for the $\omega - Zr$.

For averaging over the thickness, we use p from the Prandtl's solution Eq. (25):

$$p = -\frac{1}{3}(2\sigma_{11} + \sigma_{33}) = -\sigma_{33} - \frac{2}{3}\sigma_y \sqrt{1 - \left(\frac{mz}{h}\right)^2}. \quad (85)$$

Then

$$p^2 = \sigma_{33}^2 + \frac{4}{9}\sigma_y^2 \left(1 - \left(\frac{mz}{h}\right)^2\right) + \frac{4}{3}\sigma_{33}\sigma_y \sqrt{1 - \left(\frac{mz}{h}\right)^2}. \quad (86)$$

After averaging over the thickness we obtain:

$$\bar{p}^2 = \sigma_{33}^2 + \frac{4}{9}\sigma_y^2(\bar{p}) \left(1 - \frac{m^2}{3}\right) + \frac{4}{3}\sigma_{33}\sigma_y(\bar{p}) \frac{m\sqrt{1 - m^2} + \sin^{-1}m}{2m}. \quad (87)$$

It is clear that $\bar{p}^2 \neq \bar{p}^2$. Using Eq. (82), the average over the thickness total Lagrangian

α -Zr

Standard Rietveld refinement

a/a_0	c/c_0	V/V_0
0.996	0.995	0.988



Pressure (GPa) based on hydrostatic generalized EoS

p_a	p_c	p_V
0.987	1.463	1.138

In plane Rietveld refinement

$E_{0,rr}$	$E_{0,\theta\theta}$	$E_{0,zz}$	$E_{0,v}$
-0.0032	-0.0033	-0.0055	-0.012



Stresses (GPa) based on Hooke's law under pressure

σ_{rr}	$\sigma_{\theta\theta}$	σ_{zz}	p	$\sigma_{rr} - \sigma_{zz}$	$\sigma_y(p)$
-1.07	-1.07	-1.33	1.15	0.26	1.04

CEA

$E_{0,rr}$	$E_{0,\theta\theta}$	$E_{0,zz}$	$E_{0,v}$
-0.00325	-0.00325	-0.01647	-0.023

σ_{rr}	$\sigma_{\theta\theta}$	σ_{zz}	p	$\sigma_{rr} - \sigma_{zz}$	$\sigma_y(p)$
-1.96	-1.96	-3.24	2.39	1.28	1.28

Supplementary Fig. 4: Comparison of the stresses and elastic strains from the standard Rietveld refinement and CEA for α -Zr.

strain is

$$\bar{E}_{0,33} = \bar{\varepsilon}_{33} - 0.00664\bar{\varepsilon}_{33}\bar{p} + 0.00013\bar{\varepsilon}_{33}\bar{p}^2 + 0.5(0.00013\bar{p}^2 - 0.00664\bar{p}) \quad (88)$$

for α -Zr and

$$\bar{E}_{0,33} = \bar{\varepsilon}_{33} - 0.0066\bar{\varepsilon}_{33}\bar{p} + 0.000077\bar{\varepsilon}_{33}\bar{p}^2 + 0.5(0.000077\bar{p}^2 - 0.0066\bar{p}) \quad (89)$$

for ω -Zr. In obtaining Eqs. (88) and (89), assumptions $\frac{1}{h} \int_0^h \tilde{\varepsilon}_{33} p dz \simeq \bar{\varepsilon}_{33}\bar{p}$ and $\frac{1}{h} \int_0^h \tilde{\varepsilon}_{33} p^2 dz \simeq \bar{\varepsilon}_{33}\bar{p}^2$ are used.

3 The reasons for the difference between stresses and elastic strains from Rietveld refinement and CEA approach

To better illustrate the main sources and reasons for the difference between two approaches, let us calculate averaged over thickness stresses at the sample center, where shear strain, stresses, and m are zero, see Supplementary Fig. 4. Three approaches will be compared.

1. Using standard Rietveld refinement, the ratios of lattice parameters for the chosen sample thickness of α -Zr are $a/a_0 = 0.996$, $c/c_0 = 0.995$, and for the corresponding unit cell volume ratio $V/V_0 = 0.988$. Utilization of the experimental generalized EOSs for a , c , and V results in three different pressures, $p_a = 0.987$ GPa, $p_c = 1.463$ GPa, and $p_V = 1.138$ GPa, respectively. Difference between these values shows the inconsistency of utilizing EOS ob-

tained under hydrostatic conditions to determine pressure under non-hydrostatic conditions, especially with the axial diffraction.

2. If we use $\bar{E}_{0,rr} = -0.0032$ and $\bar{E}_{0,\theta\theta} = -0.0033$ measured experimentally (which are consistent with $a/a_0 = 0.996$ and c-axis aligned with z-axis), and determine $\bar{E}_{0,zz} = -0.0055$ to have the same $V/V_0 = 0.988$ from the standard Rietveld refinement (since $\bar{E}_{0,zz}$ does not contribute to the X-ray diffraction patterns in the axial geometry), then applying the modified pressure-dependent Hooke's law (assuming $\bar{E}_{0,rr} \approx \bar{E}_{0,\theta\theta} = 0.5(\bar{E}_{0,rr} + \bar{E}_{0,\theta\theta})$), we obtain $\sigma_{rr} = \sigma_{\theta\theta} = -1.07$ GPa, $\sigma_{zz} = -1.33$ GPa, and $p = 1.15$ GPa. Thus, p did not practically change in comparison with p_V . The main problem is that $|\sigma_{zz} - \sigma_{rr}| = 0.26$ GPa, which is much smaller than the yield strength $\sigma_y = 0.82 + 0.19 * 1.15 = 1.04$ GPa at such pressure, which is contradictory.

3. If alternatively, we use the same $\bar{E}_{0,rr} = \bar{E}_{0,\theta\theta} = -0.00325$ and determine $\bar{E}_{0,zz} = -0.01647$ from the developed CEA approach, we obtain $\sigma_{rr} = \sigma_{\theta\theta} = -1.96$ GPa, $\sigma_{zz} = -3.24$ GPa, and $p = 2.39$ GPa. The yield condition $|\sigma_{zz} - \sigma_{rr}| = \sigma_y = 0.82 + 0.19 * 2.38 = 1.28$ GPa is met, i.e., everything is consistent. The main reason for the difference of 1.24 GPa between $p = 1.15$ GPa in the approach #2 and $p = 2.39$ GPa, in which $\bar{E}_{0,zz}$ is determined with CEA to satisfy the yield condition, is that for axial XRD $\bar{E}_{0,zz}$ does not contribute to the XRD patterns, which is neglected in the traditional Rietveld refinement but is taken into account in the developed CEA method. Another conclusion is that standard Rietveld refinement for axial diffraction underestimates volumetric strain, -0.012 instead of -0.023.

Similar results for ω -Zr are presented in Supplementary Fig. 5. While difference in pressure between standard Rietveld refinement and that with CEA is significant (2.2 GPa), the pressure obtained with approach 2 is the same as with the CEA. However, stress components and especially their difference $|\sigma_{rr} - \sigma_{zz}|$ change significantly, by 1.9 GPa.

4 FEM simulations

4.1 Complete system of equations for FEM simulations [8]

Box 1 summarizes all equations derived in [8] in the form used in our simulations. Vectors and tensors are denoted in boldface type, e.g., $\mathbf{A} = A_{ij}\mathbf{e}_i\mathbf{e}_j$, where A_{ij} are components in the Cartesian system with unit basis vectors \mathbf{e}_i and summation over the repeated indices is assumed. Expressions $\mathbf{e}_i\mathbf{e}_j$ and $\mathbf{e}_i\mathbf{e}_k\mathbf{e}_t\mathbf{e}_d$ designate the direct or dyadic product of vectors, which represent second- and fourth-rank tensors, respectively. Let $\mathbf{A} \cdot \mathbf{B} = A_{ik}B_{kj}\mathbf{e}_i\mathbf{e}_j$ and $\mathbf{A} : \mathbf{B} = tr(\mathbf{A} \cdot \mathbf{B}) = A_{ij}B_{ji}$ be the contraction (or scalar product) of tensors over one and two nearest indices, where tr is the trace operation (sum of the diagonal components), and $A_{ik}B_{kj}$ is the matrix product. In the equations, first \cdot is performed, and then $:$, e.g., $\mathbf{A} : \mathbf{B} \cdot \mathbf{K} = \mathbf{A} : (\mathbf{B} \cdot \mathbf{K})$. The direct (or dyadic) product of two tensors \mathbf{K} and \mathbf{M} is the tensor \mathbf{KM} of rank equal to the sum of the two initial ranks. In particular, for the second-rank tensors $\mathbf{K} = K_{ij}\mathbf{e}_i\mathbf{e}_j$ and $\mathbf{M} = M_{kl}\mathbf{e}_k\mathbf{e}_l$, one has $\mathbf{KM} = K_{ij}M_{kl}\mathbf{e}_i\mathbf{e}_j\mathbf{e}_k\mathbf{e}_l$. Also, $\mathbf{A}_s = \frac{\mathbf{A} + \mathbf{A}^t}{2}$ and $\mathbf{A}_a = \frac{\mathbf{A} - \mathbf{A}^t}{2}$ are respectively the symmetric and anti-symmetric components of \mathbf{A} , where $'t'$ in the superscript designates the transpose operation defined as $\mathbf{A}^t = A_{ji}\mathbf{e}_i\mathbf{e}_j$, when $\mathbf{A} = A_{ij}\mathbf{e}_i\mathbf{e}_j$.

Box 1. The complete system of equations

ω -Zr

Standard Rietveld refinement

a/a_0	c/c_0	V/V_0
0.958	0.961	0.882



Pressure (GPa) based on hydrostatic generalized EoS

p_a	p_c	p_V
15.2	15.5	15.3

In plane Rietveld refinement

$E_{0,rr}$	$E_{0,\theta\theta}$	$E_{0,zz}$	$E_{0,v}$
-0.0364	-0.0377	-0.0439	-0.118



Stresses (GPa) based on Hooke's law under pressure

σ_{rr}	$\sigma_{\theta\theta}$	σ_{zz}	p	$\sigma_{rr} - \sigma_{zz}$	$\sigma_y(p)$
-17.1	-17.1	-18.3	17.5	1.2	3.1

CEA

$E_{0,rr}$	$E_{0,\theta\theta}$	$E_{0,zz}$	$E_{0,v}$
-0.03705	-0.03705	-0.06102	-0.135

σ_{rr}	$\sigma_{\theta\theta}$	σ_{zz}	p	$\sigma_{rr} - \sigma_{zz}$	$\sigma_y(p)$
-16.5	-16.5	-19.6	17.5	3.1	3.1

Supplementary Fig. 5: Comparison of the stresses and elastic strains from the standard Rietveld refinement and CEA for ω -Zr.

Decomposition of the total deformation gradient \mathbf{F} into elastic \mathbf{F}_e and inelastic \mathbf{F}_i contributions:

$$\mathbf{F} = \frac{\partial \mathbf{r}}{\partial \mathbf{r}_0} = \mathbf{V}_e \cdot \mathbf{R}_e \cdot \mathbf{U}_i = \mathbf{V}_e \cdot \bar{\mathbf{F}}_i; \bar{\mathbf{F}}_i = \mathbf{R}_e \cdot \mathbf{U}_i; \mathbf{B}_e = 0.5(\mathbf{F}_e \cdot \mathbf{F}_e^t - \mathbf{I}) = 0.5(\mathbf{V}_e^2 - \mathbf{I}), \quad (90)$$

where \mathbf{r} and \mathbf{r}_0 are respectively the position vectors of the material point in current and reference configurations. \mathbf{V}_e and \mathbf{R}_e are from the polar decomposition of \mathbf{F}_e ; \mathbf{U}_i is the right stretch tensor from the polar decomposition of \mathbf{F}_i and \mathbf{B}_e is the elastic Eulerian strain tensor. Decomposition of the deformation rate \mathbf{d} into elastic, plastic, and transformation parts:

$$\mathbf{d} = \overset{\nabla}{\mathbf{B}}_e \cdot \mathbf{V}_e^{-2} + 2(\mathbf{d} \cdot \mathbf{B}_e)_a \cdot \mathbf{V}_e^{-2} + \gamma + \bar{\varepsilon}_{t0} \dot{\mathbf{I}} \quad (91)$$

where $\overset{\nabla}{\mathbf{B}}_e = \dot{\mathbf{B}}_e - 2(\mathbf{w} \cdot \mathbf{B}_e)_s$ is the Jaumann time derivative of \mathbf{B}_e , \mathbf{w} is the anti-symmetric part of the velocity gradient in the current configuration \mathbf{l} ; γ is the plastic part of the deformation rate, $\bar{\varepsilon}_{t0}$ is the volumetric transformation strain, and \mathbf{I} is the unit tensor.

The third-order Murnaghan potential:

$$\psi(\mathbf{B}_e) = \frac{\lambda + 2G}{2} I_1^2 - 2GI_2 + \left(\frac{l + 2m}{3} I_1^3 - 2mI_1I_2 + nI_3 \right), \quad (92)$$

where λ , G , l , m , and n are the Murnaghan material constants of the mixture and I_1 , I_2 , and I_3 are the invariants of \mathbf{B}_e defined as

$$\begin{aligned} I_1 &= B_{e11} + B_{e22} + B_{e33}; \\ I_2 &= B_{e22}B_{e33} - B_{e23}^2 + B_{e11}B_{e33} - B_{e13}^2 + B_{e22}B_{e11} - B_{e12}^2; \\ I_3 &= \det(\mathbf{B}_e). \end{aligned} \quad (93)$$

A simple mixture rule is used to obtain the Murnaghan constants of the mixture

$$\begin{aligned} \lambda &= (1-c)\lambda_1 + c\lambda_2; \quad G = (1-c)G_1 + cG_2; \quad m = (1-c)m_1 + cm_2; \\ l &= (1-c)l_1 + cl_2; \quad n = (1-c)n_1 + cn_2. \end{aligned} \quad (94)$$

Here, the subscripts 1 and 2 designate α - and ω -Zr, c is the concentration of the ω -Zr.

Elasticity rule for the Cauchy (true) stress:

$$\begin{aligned} \boldsymbol{\sigma} &= J_e^{-1}(2\mathbf{B}_e + \mathbf{I}) \cdot \frac{\partial \psi}{\partial \mathbf{B}_e} \\ &= J_e^{-1}(2\mathbf{B}_e + \mathbf{I}) \cdot \left(\lambda I_1 \mathbf{I} + 2G \mathbf{B}_e + (lI_1^2 - 2mI_2) \mathbf{I} + n \frac{\partial I_3}{\partial \mathbf{B}_e} + 2mI_1 \mathbf{B}_e \right), \end{aligned} \quad (95)$$

where $J_e = \det \mathbf{F}_e$ is the Jacobian determinant of \mathbf{F}_e . Compact expressions of $\frac{\partial I_1}{\partial \mathbf{B}_e}$, $\frac{\partial I_2}{\partial \mathbf{B}_e}$, and $\frac{\partial I_3}{\partial \mathbf{B}_e}$ are

$$\frac{\partial I_1}{\partial \mathbf{B}_e} = \mathbf{I}; \quad \frac{\partial I_2}{\partial \mathbf{B}_e} = -\mathbf{B}_e + I_1 \mathbf{I}; \quad \frac{\partial I_3}{\partial \mathbf{B}_e} = \mathbf{B}_e \cdot \mathbf{B}_e - I_1 \mathbf{B}_e + I_2 \mathbf{I}. \quad (96)$$

Yield surface:

$$\phi = \sqrt{3/2} \mathbf{s} : \mathbf{s} - (\sigma_{y0} + bp) = 0; \quad \sigma_{y0} = (1-c)\sigma_{y01} + c\sigma_{y02}; \quad b = (1-c)b_1 + cb_2. \quad (97)$$

Here, \mathbf{s} is the deviatoric part of the Cauchy stress $\boldsymbol{\sigma}$, p is the pressure, σ_{y01} and σ_{y02} are the yield strengths in compression of the α - and ω -Zr @ $p = 0$, respectively, b_1 and b_2 are their linear pressure hardening coefficients.

Plastic flow rule:

$$\boldsymbol{\gamma} = |\boldsymbol{\gamma}| \frac{\mathbf{s}}{\sqrt{\mathbf{s} : \mathbf{s}}} = |\boldsymbol{\gamma}| \mathbf{n}; \quad |\boldsymbol{\gamma}| = (\boldsymbol{\gamma} : \boldsymbol{\gamma})^{0.5} \text{ when } \phi(\mathbf{s}, p, c) = 0 \text{ and } \dot{\phi}(\mathbf{s}, p, c) = 0, \quad (98)$$

i.e., in the elastoplastic region, and $|\boldsymbol{\gamma}|$ is determined from the consistency condition $\dot{\phi}(\mathbf{s}, p, c) = 0$; where $|\boldsymbol{\gamma}| = 0$ in the elastic region when $\phi(\mathbf{s}, p, c) < 0$ or $\phi(\mathbf{s}, p, c) = 0$ and $\dot{\phi}(\mathbf{s}, p, c) = 0$.

$$|\boldsymbol{\gamma}| = \frac{-\left(\frac{\sqrt{1.5}\mathbf{s}}{\sqrt{\mathbf{s} : \mathbf{s}}} + \frac{b}{3}\mathbf{I}\right) : \mathbf{Y}}{\left(\frac{\sqrt{1.5}\mathbf{s}}{\sqrt{\mathbf{s} : \mathbf{s}}} + \frac{b}{3}\mathbf{I}\right) : \mathbf{Z} + \frac{\partial \phi}{\partial c} A \sqrt{\frac{2}{3}}} : \mathbf{d} \quad (99)$$

where $\mathbf{Y} = \frac{\partial \boldsymbol{\sigma}}{\partial \mathbf{B}_e} \cdot \mathbf{V}_e^2$, $\mathbf{Z} = -\mathbf{Y} : \left[\mathbf{n} + (\bar{\varepsilon}_{t0} \mathbf{I} + \boldsymbol{\gamma}_t) A \sqrt{\frac{2}{3}} + \frac{\partial f}{\partial c} A \sqrt{\frac{2}{3}} \right]$, $\boldsymbol{\sigma} = \mathbf{f}(\mathbf{B}_e, c)$, and $\frac{dc}{dq} = A(p, q, c)$.

Accumulated plastic strain:

$$\dot{q} = \sqrt{2/3} |\boldsymbol{\gamma}| \quad (100)$$

Stress rate – deformation rate relationship:

$$\overset{\nabla}{\boldsymbol{\sigma}} = \left(\mathbf{Y} + \mathbf{Z} \frac{-\left(\frac{\sqrt{1.5}s}{\sqrt{s:s}} + \frac{b}{3} \mathbf{I}\right) : \mathbf{Y}}{\frac{\partial \phi}{\partial \boldsymbol{\sigma}} : \mathbf{Z} + \left(\frac{\partial \phi}{\partial c} A + \frac{\partial \phi}{\partial q}\right) \sqrt{\frac{2}{3}}} \right) : \mathbf{d} \quad (101)$$

Equilibrium equation:

$$\nabla \cdot \boldsymbol{\sigma} = \mathbf{0} \quad (102)$$

4.2 Geometry and boundary conditions

Geometry of DAC is shown in see Fig. 1a in the main text. Axisymmetric problem formulation is considered. Geometry of the sample and the anvil, as well as the boundary conditions, are shown in see Supplementary Fig. 6. They are:

(1) A uniform vertical displacement is applied at the boundary between the top inclined surface of the anvil and Bohler-type seat (line CD). Distributions of stresses or displacements along this surface do not affect fields in the sample and the diamond close to the diamond culet.

(2) At the symmetry axis $r = 0$ (line AB), τ_{rz} and horizontal displacement are zero. At the symmetry plane $z = 0$, shear stress τ_{rz} and vertical displacement are zero.

(3) At the contact surface between the sample and the anvil, an isotropic friction model, described below, is utilized.

(4) Other surfaces not mentioned above are stress-free. Quadrilateral 4-node bilinear axisymmetric finite elements CGAX4R are used in simulations, which are commonly used for large-deformation axisymmetric problems [9]. Our simulations utilize a mesh with 4271 elements.

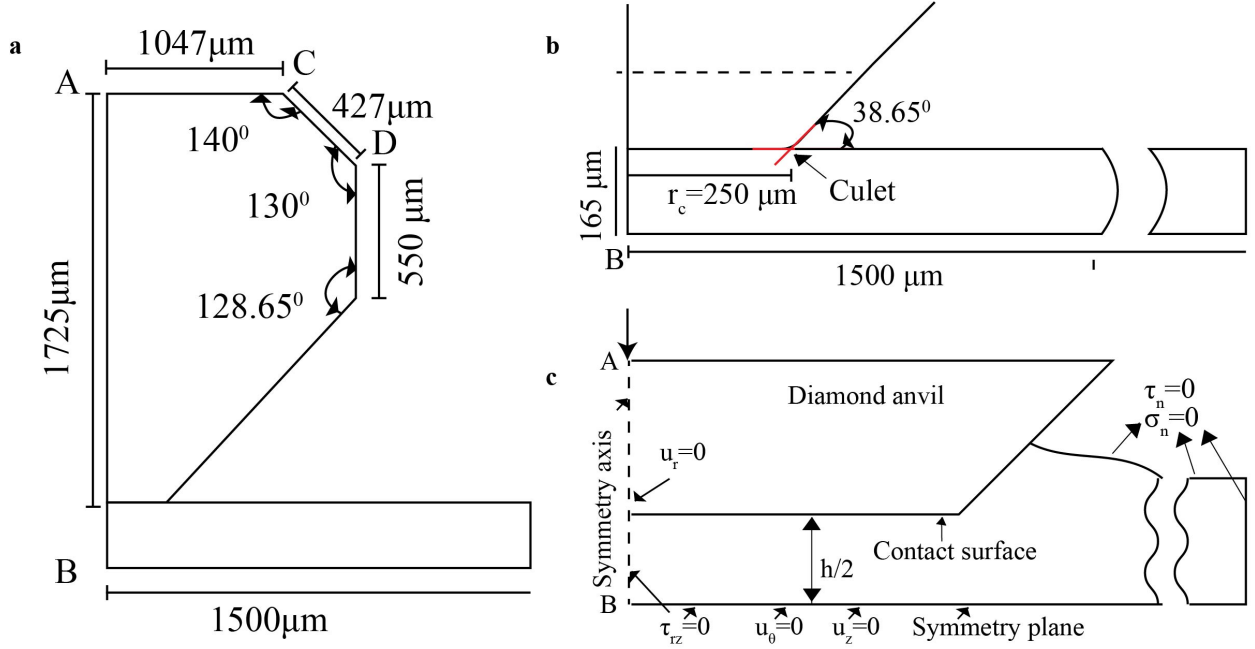
Evolution of concentration of ω phase $c(r)$ and corresponding volumetric transformation strain $\bar{\varepsilon}_{t0} \dot{\mathbf{c}} \mathbf{I}$ ($\bar{\varepsilon}_{t0} = -0.0158$) are introduced homogeneously along the z-coordinate in our FEM problem formulation for each loading step.

Friction model:

At the culet portion of the diamond $r \leq r_c$, the contact shear stress is given by

$$\tau_c = m' \tau_y(p) \quad \text{for } r \leq r_c \quad (103)$$

The distribution of $m'(r)$ is obtained from the analytical solution (Supplementary Fig. 7).



Supplementary Fig. 6: **Details of the geometrical model of the DAC experiment used in FEM:** **a** Description of the one half of diamond dimensions in the natural configuration. **b** Geometric parameters of one half of sample and the angle between culet and non-culet diamond surfaces. **c** Boundary conditions and the schematic of sample in the deformed configuration.

At the inclined portion of the sample-diamond contact surface, the critical shear is governed by the combined Coulomb friction $\tau_{cr} = \mu(\sigma_c)\sigma_c$ and Eq. (103), where σ_c is the contact normal stress. There is complete cohesion between the sample and the anvil unless shear stress τ_c reaches the critical value:

$$\tau_c < \tau_{cr} = \min[\mu(\sigma_c)\sigma_c, m'(r_c)\tau_y(p)] \rightarrow \text{cohesion}, \quad (104)$$

where $m' = m'(r_c)$ is determined at $r = r_c$. When friction stress reaches τ_{cr} ,

$$\tau_c = \tau_{cr} = \min[\mu(\sigma_c)\sigma_c, m'(r_c)\tau_y(p)] \rightarrow \text{sliding}, \quad (105)$$

contact sliding occurs.

4.3 Nonlinear elastic equations and material properties for single-crystal diamond anvil

The constitutive response of diamond is modeled using fourth-order nonlinear anisotropic elastic potential energy given by Vekilov et al. [10]:

$$\begin{aligned}
\psi = & \frac{1}{2}c_{11}(\eta_1^2 + \eta_2^2 + \eta_3^2) + c_{12}(\eta_1\eta_2 + \eta_2\eta_3 + \eta_1\eta_3) + \frac{1}{2}c_{44}(\eta_4^2 + \eta_5^2 + \eta_6^2) + \frac{1}{6}c_{111}(\eta_1^3 + \eta_2^3 + \eta_3^3) \\
& + \frac{1}{2}c_{112}[\eta_1^2(\eta_2 + \eta_3) + \eta_2^2(\eta_1 + \eta_3) + \eta_3^2(\eta_1 + \eta_2)] + c_{123}\eta_1\eta_2\eta_3 + c_{456}\eta_4\eta_5\eta_6 + \\
& \frac{1}{2}c_{144}(\eta_1\eta_4^2 + \eta_2\eta_5^2 + \eta_3\eta_6^2) + \frac{1}{2}c_{155}[\eta_4^2(\eta_2 + \eta_3) + \eta_5^2(\eta_1 + \eta_3) + \eta_6^2(\eta_1 + \eta_2)] + \\
& \frac{1}{24}c_{1111}(\eta_1^4 + \eta_2^4 + \eta_3^4) + \frac{1}{6}c_{1112}[\eta_1^3(\eta_2 + \eta_3) + \eta_2^3(\eta_1 + \eta_3) + \eta_3^3(\eta_1 + \eta_2)] + \frac{1}{4}c_{1144}(\eta_1^2\eta_4^2 + \\
& \eta_2^2\eta_5^2 + \eta_3^2\eta_6^2) + \frac{1}{4}c_{1122}(\eta_1^2\eta_2^2 + \eta_2^2\eta_3^2 + \eta_3^2\eta_1^2) + \frac{1}{2}c_{1123}\eta_1\eta_2\eta_3(\eta_1 + \eta_2 + \eta_3) + \\
& \frac{1}{4}c_{1155}[\eta_1^2(\eta_6^2 + \eta_5^2) + \eta_2^2(\eta_6^2 + \eta_4^2) + \eta_3^2(\eta_5^2 + \eta_4^2)] + \frac{1}{2}c_{1255}[\eta_1\eta_2(\eta_4^2 + \eta_5^2) + \eta_3\eta_2(\eta_6^2 + \\
& \eta_5^2) + \eta_1\eta_3(\eta_6^2 + \eta_4^2)] + \frac{1}{2}c_{1266}(\eta_1\eta_2\eta_6^2 + \eta_2\eta_3\eta_4^2 + \eta_1\eta_3\eta_5^2) + c_{1456}\eta_4\eta_5\eta_6(\eta_1 + \eta_2 + \eta_3) + \\
& \frac{1}{24}c_{4444}(\eta_4^4 + \eta_5^4 + \eta_6^4) + \frac{1}{4}c_{4455}(\eta_4^2\eta_5^2 + \eta_6^2\eta_5^2 + \eta_4^2\eta_6^2),
\end{aligned} \tag{106}$$

where $\eta_1 = E_{e11}$, $\eta_2 = E_{e22}$, $\eta_3 = E_{e33}$, $\eta_4 = 2E_{e23}$, $\eta_5 = 2E_{e31}$, and $\eta_6 = 2E_{e12}$ are the Lagrangian strains. Based on the elasticity law, the Cauchy stress in the diamond can be obtained using:

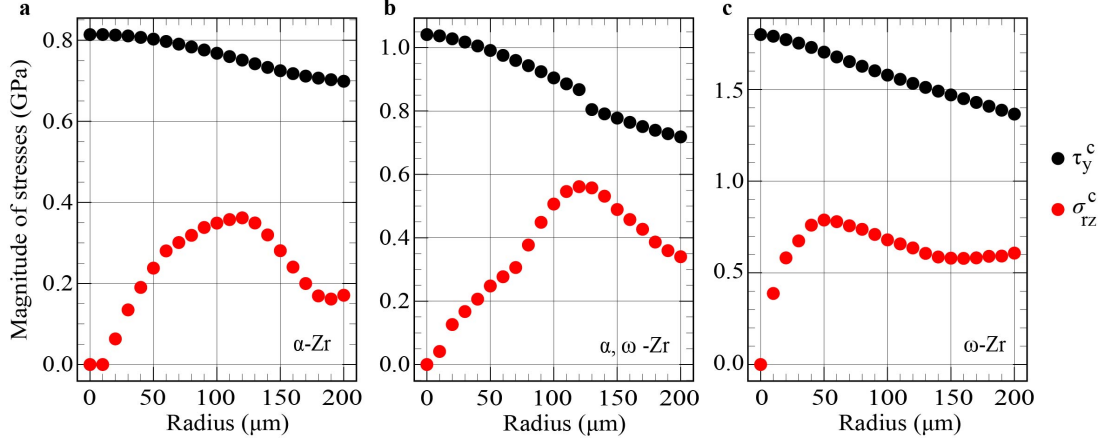
$$\boldsymbol{\sigma} = \frac{1}{J} \mathbf{F}_e \cdot \frac{\partial \psi}{\partial \mathbf{E}_e} \cdot \mathbf{F}_e^t. \tag{107}$$

Here J is the Jacobian determinant of \mathbf{F}_e . All the elastic constants of diamond are taken from Telichko et al. [11] and they are as follows (all in GPa):

$$\begin{aligned}
c_{11} &= 1081.9, c_{12} = 125.2, c_{44} = 578.6; \\
c_{111} &= -7611, c_{112} = -1637, c_{123} = 604, c_{144} = -199, c_{166} = -2799, c_{155} = -2799, \\
c_{456} &= -1148, c_{1111} = 26687, c_{1112} = 9459, c_{1122} = 6074, c_{1123} = -425, c_{1144} = -1385, \\
c_{1155} &= 10741, c_{1255} = -264, c_{1266} = 8192, c_{1456} = 487, c_{4444} = 11328, c_{4455} = 528.
\end{aligned} \tag{108}$$

4.4 Elastic properties of polycrystalline α - and ω -Zr

The elastic constitutive response of polycrystalline Zr is modeled using the third-order nonlinear Murnaghan potential Eq. (92). Out of 5 elastic constants in the Murnaghan potential, 2 elastic constants, Lamé constant λ and shear modulus G , are related to the quadratic in \mathbf{B}_e terms, and the rest, l , m and n , are related to the cubic in \mathbf{B}_e terms. These constants are calibrated using the bulk modulus K and its pressure derivative $\frac{dK}{dp}@p=0$ obtained from the pressure-volume relationships in hydrostatic DAC experiments, and the shear modulus G and its pressure-derivative $\frac{dG}{dp}@p=0$ are taken from the experimental results [12, 13]. The



Supplementary Fig. 7: **Radial distributions of shear stress and yield strength in shear a** for pure α -Zr, **b** for the mixture of α - and ω -Zr and **c** for the pure ω -Zr obtained using an analytical model and experimentally measured radial $\bar{E}_{0,rr}$ and azimuthal $\bar{E}_{0,\theta\theta}$ strain distributions.

expressions relating the Murnaghan constants λ , G , l , m , n and K , G , $\frac{dK}{dp}$ and $\frac{dG}{dp}$ @ $p = 0$ are:

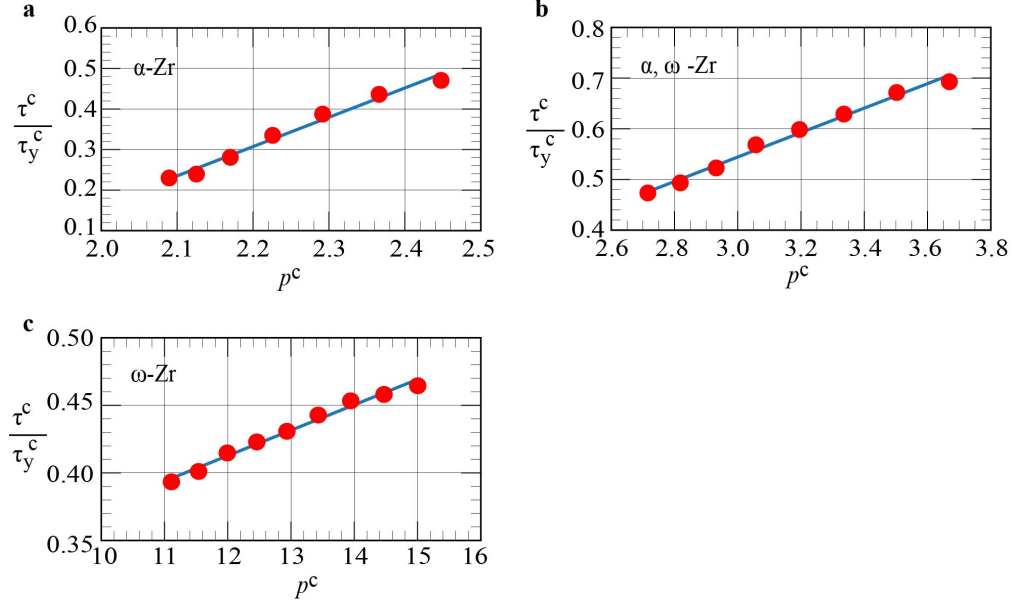
$$K = \frac{3\lambda + 2G}{3}; \quad \frac{dK}{dp} = K' = -\frac{2(9l + n)}{9K}; \quad \frac{dG}{dp} = G' = \frac{-2G - 6K - 6m + n}{6K}. \quad (109)$$

It can be seen there are only 2 equations to solve for the 3 third-order constants. Therefore, there is an indeterminacy of degree 1. However, it can be easily shown for any pressure, that when the deviatoric part of the superposed deformation is small, the stresses and energy can be written in terms of just K , G , K' , and G' . Therefore, one of the constants, l , m , or n , can be chosen arbitrarily, and the other two are determined from Eq. (109). The constants that are used are (all in GPa):

$$\begin{aligned} \lambda = 68.11, \quad G = 36.13, \quad l = -147.01, m = -122.75, \quad n = -100 & \quad \text{for } \alpha - \text{Zr}; \\ \lambda = 72.33, \quad G = 45.1, \quad l = -149.56, m = -179.53, \quad n = -4 & \quad \text{for } \omega - \text{Zr}. \end{aligned} \quad (110)$$

5 Friction stress and rules for α and ω Zr and their mixture

Friction along the sample-diamond contact surface in the DAC experiment plays a central role in generating high pressure in the sample. However, the magnitude of the friction force along the contact surface cannot be measured. Traditionally [5, 14, 15], the yield strength in shear was assumed to be equal to the sliding friction force. But it was reported recently in [16, 17] that the sliding friction force is significantly lower than the yield strength in shear. This important deduction, coupled with the elusive nature of the mechanism of the sliding friction at high pressure, posed an important problem to find boundary conditions for FEM solution and increased the degree of indeterminacy of all fields in a sample. The problem is resolved by using the results of analytical model that gives the distributions of contact shear stress (Supplementary Fig. 7). For the mixture of $\alpha+\omega$ Zr, there is a jump in yield strength in shear of mixture, which is due to the jump in the concentration of the ω -Zr phase (See Fig. 2 in main text).

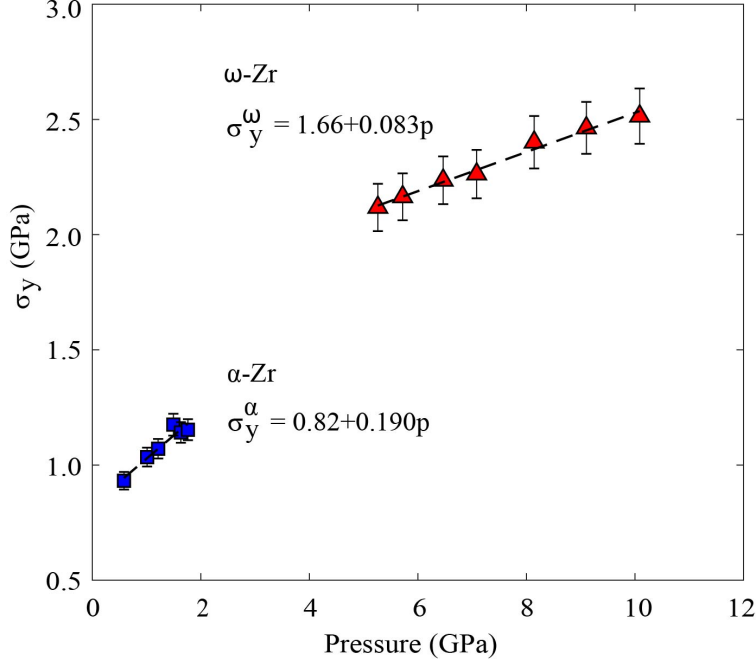


Supplementary Fig. 8: **Pressure dependence of the contact friction stress τ_c normalized by the yield strength in shear τ_y^c at the same point.** Results are presented for **a** pure α -Zr at $p_{max} = 3.09$ GPa, **b** mixture of α - and ω -Zr at $p_{max} = 4.77$ GPa, and **c** pure ω -Zr at $p_{max} = 17.55$ GPa.

To find friction sliding laws, we must exclude regions near the symmetry axis. At the symmetry axis, friction stress is zero due to symmetry, which leads to zero or very small sliding near the symmetry. We also exclude region near the culet edge, where character of the plastic flow significantly changes.

The best linear fits for the contact friction stress τ_c normalized by the yield strength in shear τ_y^c at the same point for pure- ω Zr in the region $r = 60 \mu m$ to $140 \mu m$, for the mixture of α and ω Zr in the region $r = 130 \mu m$ to $200 \mu m$, and for the pure- α Zr in the region $r = 130 \mu m$ to $190 \mu m$ are (Supplementary Fig. 8):

$$\begin{aligned}
 \left(\frac{\tau_c}{\tau_y^c} \right)_{\omega} &= 0.186 + 0.018p^c \quad \text{for } 11.1 \leq p^c(\text{GPa}) \leq 15.0; \quad 60 \leq r(\mu m) \leq 140; \\
 \left(\frac{\tau_c}{\tau_y^c} \right)_{\alpha+\omega} &= 0.179 + 0.241p^c \quad \text{for } 2.7 \leq p^c(\text{GPa}) \leq 3.7; \quad 130 \leq r(\mu m) \leq 200; \\
 \left(\frac{\tau_c}{\tau_y^c} \right)_{\alpha} &= -1.282 + 0.722p^c \quad \text{for } 2.0 \leq p^c(\text{GPa}) \leq 2.45; \quad 130 \leq r(\mu m) \leq 190;
 \end{aligned} \tag{111}$$



Supplementary Fig. 9: **Pressure dependence of yield strength in compression of α - and ω -Zr.**

6 Pressure-dependence of the yield strengths of α and ω Zr

The yield strengths of α and ω phases of Zr were estimated using the peak broadening method [1] near the center of a sample (see Supplementary Fig. 9):

$$\sigma_y^\alpha = 0.82 + 0.19p \text{ (GPa)} \quad \text{and} \quad \sigma_y^\omega = 1.66 + 0.083p \text{ (GPa)}$$

It is worth mentioning here that Zhao et al. [1] reported the yield strengths of α and ω phases as 0.18 GPa and 1.18 GPa at ambient pressure, respectively. The reason that our values of the yield strengths are significantly higher is that our Zr sample was subjected to large preliminary plastic deformation until saturation of the strain hardening, while Zhao et al. performed experiments on an annealed Zr sample.

7 Equation of state under hydrostatic loading

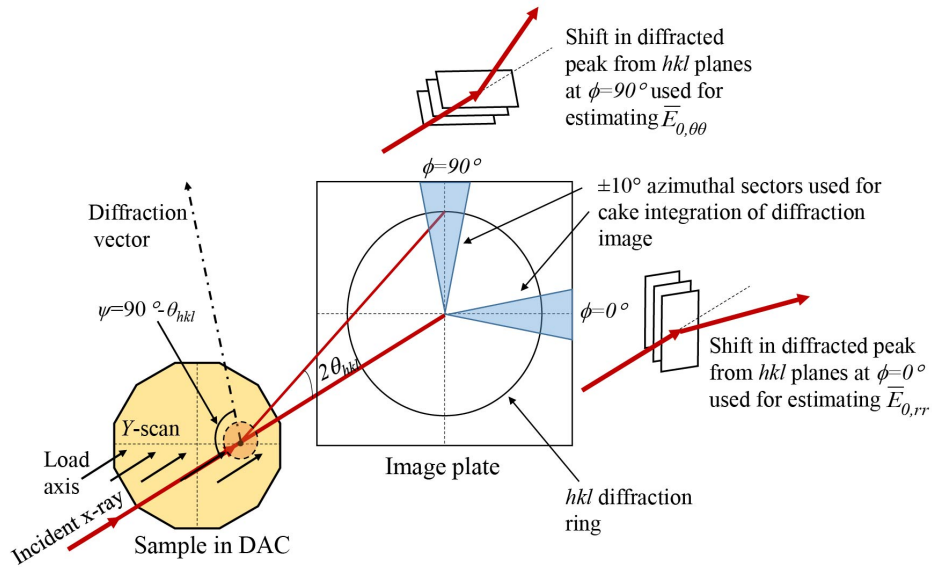
Experiments under hydrostatic loading were performed for comparison and to determine the equation of state for both phases. The $\alpha \rightarrow \omega$ PT started at pressure 5.4 GPa and finished at 6.6 GPa. The 3rd order Birch-Murnaghan equation of state (EOS) fitting of pressure-volume data for α and ω phases of Zr provides: initial (ambient) volumes $V_0 = 23.269 \text{ \AA}^3$ and 34.306 \AA^3 (per formula unit); bulk moduli $K_0 = 93.55 \text{ GPa}$ and 102.4 GPa @ $p = 0$, and pressure derivative of bulk moduli $K' = 3.0$ and 2.93 @ $p = 0$, respectively. ω -Zr is retained at ambient pressure on complete pressure release. Components of the deformation gradient $\mathbf{F}_*(p)$ determined in the hydrostatic experiments for α and ω phases are presented in Eqs. (4)- (7).

Supplementary figures

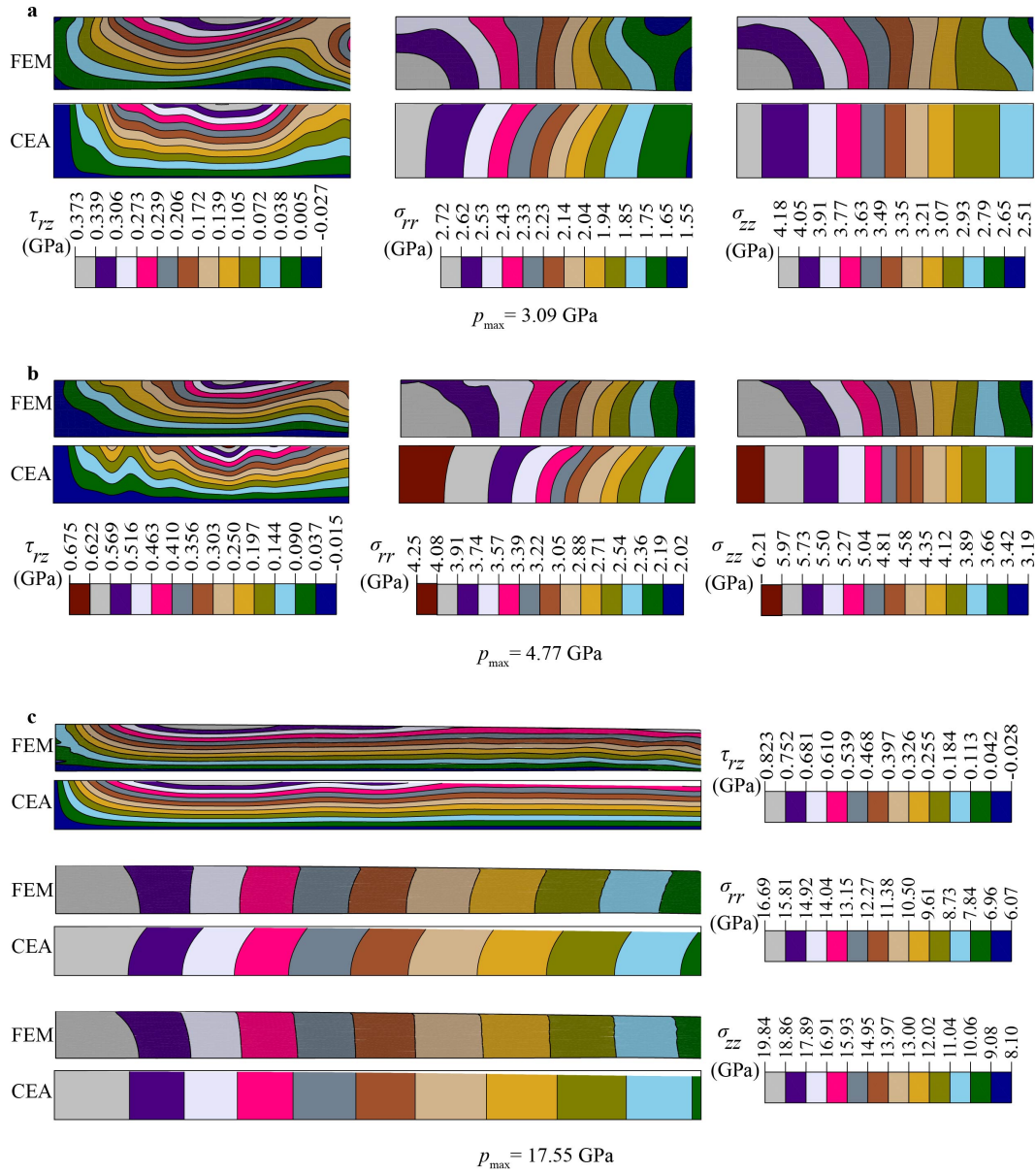
Supplementary Fig. 10: Schematic illustration of estimation of elastic strains in radial $E_{0,rr}$ and azimuthal directions $E_{0,\theta\theta}$.

Supplementary Fig. 11: 2D stress contours for 3 loading cases.

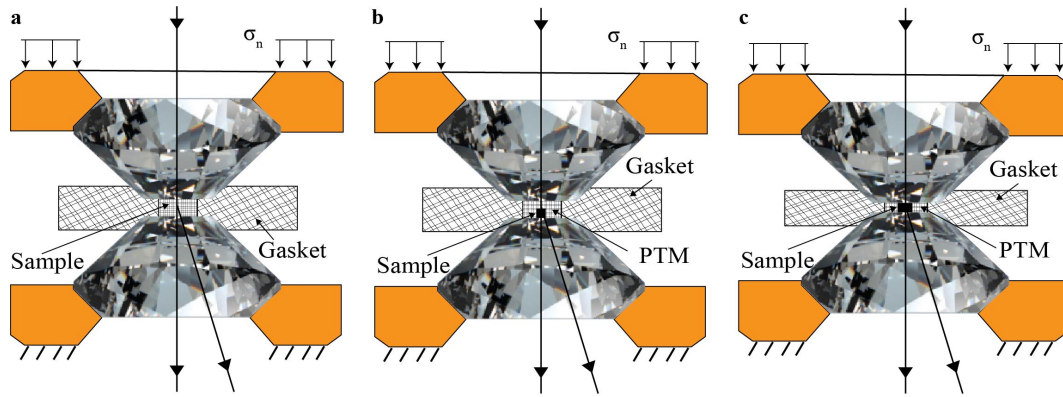
Supplementary Fig. 12: Schematics of DAC assemblies for which the developed approach is applicable.



Supplementary Fig. 10: **Schematic illustration of estimation of elastic strains in radial $\bar{E}_{0,rr}$ and azimuthal $\bar{E}_{0,\theta\theta}$ directions at each scanning position.**



Supplementary Fig. 11: **2D stress contours for three loading cases from FEM and analytical solutions.** **a** Results for almost pure $\alpha - Zr$ at $p_{max} = 3.09$ GPa. **b** Results for mixture of $\alpha -$ and $\omega - Zr$ at $p_{max} = 4.77$ GPa. **c** Results for pure $\omega - Zr$ at $p_{max} = 17.55$ GPa.



Supplementary Fig. 12: **Schematics of DAC assemblies for which the developed approach is applicable.** **a** Solid sample within a gasket without a hydrostatic medium (e.g., like in [18,19] with FEM simulations in [20] or any powder material). **b** Solid sample within a gasket with hydrostatic pressure-transmitting medium (PMT) after their solidification (e.g., like in [21–24]). **c** The same as in b but after the sample is directly compressed by anvils, from the beginning or above some load (e.g., like in [18,21,25,26]). All fields in the solidified pressure-transmitting medium and gasket can be studied in the same experiment. The developed approach can be extended for rotational DAC when torque is applied in (a)-(c).

Supplementary References

- [1] Zhao, Y. & J. Zhang, Enhancement of yield strength in zirconium metal through high-pressure induced structural phase transition. *Applied Physics Letters*, **91**, 201907 (2007).
- [2] Levitas, V.I. Nonlinear elasticity of prestressed single crystals at high pressure and various elastic moduli. *Physical Review B* **104**, 214105 (2021).
- [3] Fisher, E. S., Manghnani, M. H., & Sokolowski, T. J. Hydrostatic Pressure Derivatives of the Single-Crystal Elastic Moduli of Zirconium. *J. Appl. Phys.* **41**, 2991 (1970).
- [4] Burakovsky, L. private communication (2021).
- [5] Levitas, V. I. Large Deformation of Materials with Complex Rheological Properties at Normal and High Pressure (Nova Science Publishers, New York, 1996).
- [6] Lin F., Levitas V.I., Pandey K.K., Yesudhas S., & Park C. Laws of high-pressure phase and nanostructure evolution and severe plastic flow. DOI: <https://doi.org/10.21203/rs.3.rs-1998605/v1> (2022).
- [7] Hill, R.. The Mathematical Theory of Plasticity (Oxford University Press, Oxford, 1998).
- [8] Feng, B. & Levitas, V. I. Coupled elastoplasticity and plastic strain-induced phase transformation under high pressure and large strains: Formulation and application to BN sample compressed in a diamond anvil cell. *Int. J. Plast.* **96**, 156-181 (2017).
- [9] Dunne, F. & Petrinic, N. Introduction to computational plasticity (OUP Oxford, 2005).
- [10] Vekilov, Y. K., Krasilnikov, O. M. & Lugovskoy, A. V. Elastic properties of solids at high pressure. *Physics-Uspekhi*, **58**, 1106 (2015).
- [11] Telichko, A. V., Erohin, S. V., Kvashnin, G. M., Sorokin, P. B., Sorokin, B. P. & Blank, V. D. Diamond's third-order elastic constants: Ab initio calculations and experimental investigation. *Journal of materials science*, **52**, 3447-3456 (2017).
- [12] Liu, W., Li, B., Wang, L., Zhang, J. & Zhao, Y. Elasticity of ω -phase zirconium. *Physical Review B*, **76**, 144107 (2007).
- [13] Liu, W., Li, B., Wang, L., Zhang, J. & Zhao, Y. Simultaneous ultrasonic and synchrotron x-ray studies on pressure induced α - ω phase transition in zirconium. *Journal of Applied Physics*, **104**, 076102 (2008).
- [14] Jeanloz, R., Godwal, B. K. & Meade, C. Static strength and equation of state of rhenium at ultra-high pressures. *Nature* **349**, 687-689 (1991).
- [15] Meade, C. & Jeanloz, R. The strength of mantle silicates at high-pressures and room-temperature - implications for the viscosity of the mantle. *Nature* **348**, 533-535 (1990).

- [16] Levitas, V. I., Kamrani, M. & Feng, B. Tensorial stress-strain fields and large elasto-plasticity as well as friction in diamond anvil cell up to 400 GPa. *NPJ Computational Materials* **5**, 94 (2019).
- [17] Pandey, K. K. & Levitas, V. I. In situ quantitative study of plastic strain-induced phase transformations under high pressure: Example for ultra-pure Zr. *Acta Materialia*, **196**, 338-346 (2020).
- [18] Jenei, Z., O'Bannon, E. F., Weir, S. T., Cynn, H., Lipp, M. J. & Evans, W. J. Single crystal toroidal diamond anvils for high pressure experiments beyond 5 megabar. *Nature communications* **9**, 3563 (2018).
- [19] Ji, C., Levitas, V. I., Zhu, H., Chaudhuri, J., Marathe, A. & Ma, Y. Shear-induced phase transition of nanocrystalline hexagonal Boron Nitride to Wurtzitic structure at room temperature and low pressure. *Proceedings of the National Academy of Sciences of the United States of America* **109**, 19108-19112 (2012).
- [20] Feng, B. & Levitas, V. I. Pressure self-focusing effect and novel methods for increasing the maximum pressure in traditional and rotational diamond anvil cells. *Sci. Rep.* **7**, 45461 (2017).
- [21] Dubrovinsky, L., Dubrovinskaia, N., Prakapenka, V. B. & Abakumov, A. M. Implementation of micro-ball nanodiamond anvils for high-pressure studies above 6 Mbar. *Nature Communications* **3**, 1163 (2012).
- [22] Dias, R. P. & Silvera, I. F. Observation of the Wigner-Huntington transition to metallic Hydrogen. *Science* **355**, 715-718 (2017).
- [23] Barge, N. V. & Boehler, R. Effect of non-hydrostaticity on the α - ϵ transition of Iron. *High Pressure Research* **6**, 133-140 (2006).
- [24] Hsieh, S., Bhattacharyya, P., Zu, C., Mittiga, T., Smart, T. J., Machado, F., Kobrin, B., Höhn, T. O., Rui, N. Z., Kamrani, M., Chatterjee, S., Choi, S., Zaletel, M., Struzhkin, V. V., Moore, J. E., Levitas, V. I., Jeanloz, R. & Yao, N. Y. Imaging stress and magnetism at high pressures using a nanoscale quantum sensor. *Science* **366**, 1349-1354 (2019).
- [25] Dubrovinsky, L., Khandarkhaeva, S., Fedotenko, T., Laniel, D., Bykov, M., Giacobbe, C., Lawrence Bright, E., Sedmak, P., Chariton, S., Prakapenka, V., Ponomareva, A. V., Smirnova, E. A., Belov, M. P., Tasnadi, F., Shulumba, N., Trybel, F., Abrikosov, I. A. & Dubrovinskaia, N. Materials synthesis at terapascal static pressures. *Nature* **605**, 274-278 (2022).
- [26] Ding, Y., Sun, Y., Jiang, S., Huang, X. & Cui, T. Frontier in the diamond anvil cell techniques for ultrahigh pressure generation. *Journal of Physics: Condensed Matter* **35**, 313002 (2023).

Peer Review File

Tensorial stress-plastic strain fields in α - ω Zr mixture, transformation kinetics, and friction in diamond anvil cell



Open Access This file is licensed under a Creative Commons Attribution 4.0 International License, which permits use, sharing, adaptation, distribution and reproduction in any medium or format, as long as you give appropriate credit to the original author(s) and the source, provide a link to the Creative Commons license, and indicate if changes were made. In the cases where the authors are anonymous, such as is the case for the reports of anonymous peer reviewers, author attribution should be to 'Anonymous Referee' followed by a clear attribution to the source work. The images or other third party material in this file are included in the article's Creative Commons license, unless indicated otherwise in a credit line to the material. If material is not included in the article's Creative Commons license and your intended use is not permitted by statutory regulation or exceeds the permitted use, you will need to obtain permission directly from the copyright holder. To view a copy of this license, visit <http://creativecommons.org/licenses/by/4.0/>.

REVIEWER COMMENTS

Reviewer #1 (Remarks to the Author):

This is a very 'solid' report that attempts to bring several simulations and experimental data together to answer a very long standing question regarding the interplay between stresses, plastic strain and pressure measurement. The authors apply it to the long studied (and probably the problem that raises questions with every study) alpha-omega transition in Zr. The current manuscript also tries to evaluate a plethora of studies that are arising out of shear devices like the rotational diamond anvil cell (RDAC). In fact, this study highlights the pitfalls of studies with RDAC that can end up being highly irreproducible since improper characterization of the stress fields leads to improper estimation of pressure. This is highlighted with simulations and careful experimental data on the radial pressure distributions at various peak pressures that are validated by FEM calculations. I have no hesitation in recommending this for publication as is. This research would be followed by many high pressure researchers from as diverse a field as rock mechanics to additively manufactured materials. I do have a few questions for the authors.

(1) A large part of the simulations assume equilibrium conditions (Reuss limit). How sure are the authors that their experiments have actually attained equilibrium? I know they show great equivalence between theory and experiment but I was wondering if this is incidental or global.

(2) One of the vexing questions in elastic-plastic deformation studies in a DAC has been the Reuss-Voight interplay and in the past, there has been discussion on how particle size affects this at high packing density and shear. Can the authors comment on this especially in view of their CEA approach.

Reviewer #2 (Remarks to the Author):

The authors present a coupled experimental-analytical and experimental-analytical-computational approach for unraveling stress distributions in compression experiments with diamond anvil cells (DAC). The approach may be applied to a) assessing phase boundaries, b) understanding kinetic boundaries in the s.c. rotational DAC, that is: rotational shear experiments with extreme stress gradients.

The approach is interesting, yet it addresses problems specific to a few types of experiments with the DAC, but it does not apply any longer to DAC experiments in general: The community has turned to compression of single crystal specimens in hydrostatic and nearly hydrostatic media which remove much of the issues addressed by the authors here. Furthermore, Laue diffraction and multicrystal indexation approaches allow for assessing strain of individual crystallites in polycrystals. The use of nearly hydrostatic media like neon and helium is now common practice. Ultrahigh compression experiments on simple metals and ruby show that deviations from hydrostaticity are low up to 40-50 GPa, and for most materials tolerable (within +/- 5 GPa) to beyond 100 GPa. The experiment that the authors show in Fig 1 falls back beyond the diamond cell experiment design that has been established over the past decade.

The approach proposed by the authors has its merits and is useful for some experiments, but it is not sufficiently general nor do the authors present a case of sufficiently general scientific importance that would justify publication in Nat. Com (the alpha-omega boundary in Zr is now quite well assessed). I recommend the authors to consider a more topical journal like J. Synch. Rad. High Pressure Research, Rev. of Sci. Instr.

I add a list of comments jotted down during reading the manuscript, with the hope that they may be helpful for the authors:

. 'However, they could not be [L] [SEP] [L] measured. Even measured pressure distribution contains significant error.' (lines 9-12) [L] [SEP] [L]
-> This statement is not quite up to date (nor are the references): Recent Laue diffraction experiments across the phase transition boundary quantify strain. The corresponding stress requires independent assessment of the elastic tensor, of course.

. the most advanced characterization of the pressure conditions in a sample is based [L] [SEP] [L]
. 35 on determining the radial distribution of pressure averaged over the sample thickness using volume [L] [SEP] [L]
. 36 of a crystal cell measured by X-ray diffraction (XRD) and equation of state (EOS) determined [L] [SEP] [L]
. 37 under hydrostatic conditions4,5,8. [L] [SEP] [L]
-> Again, this is NOT the 'most advanced' characterization! Instead, single crystals of either phase should be used or domains of twinned crystals should be indexed. This is well possible in diamond cells. There are new approaches of multicrystal indexation where the UB matrices of each or most grains are assessed - both for white and monochromatic XRD.

. However, EOS for hydrostatic and nonhydrostatic loadings are [L] [SEP] [L]
. 38 quite different9-12. [L] [SEP] [L]

-> A nonhydrostatic loading does not actually give different isotherms, only if non-hydrostatic strain and stress remain unquantified, the isotherms appear to deviate
The authors are aware of this, but the wording is confusing.

. More importantly, for the XRD beam along the symmetry axis of the DAC [L] [SEP] [L]
. 39 (axial XRD), crystallographic planes that are almost parallel to the beam contribute to the [L] [SEP] [L]

. 40 measured XRD patterns only, and axial elastic strain $E_{0,zz}$ and consequently stress σ_{zz} do not
. 41 contribute to the pressure, leading to large error (bar over the field variables means averaged over
[SEP]
. 42 the sample thickness). In addition, numerous physical, chemical, geological, and mechanical [SEP]

-> This is true for non-hydrostatic experiments. The alpha-omega transition in Zr is at a pressure that is well within a regime where hydrostatic pressure can be achieved with neon or helium as pressure-transmitting media in a diamond anvil cell. The authors are referring to problems specific to non-optimal experiments or outdated approaches. The authors' approach is useful for analysing data obtained with the s.c. rotational DAC.

. The only paper that claims measurement of radial distribution of all components of the [SEP]
. 65 stress tensor is ref. 40. [SEP]

-> I don't understand this statement. There are numerous published studies on samples compressed in diamond cells under hydrostatic conditions, i.p. on single crystals. This includes studies where elastic tensors were measured with Brillouin spectroscopy along with single crystal diffraction data or axial compressibilities were assessed from single crystal compression data.

The authors address a problem of specific experiments and samples, it is not a general problem and it appears the authors are not aware of much of the recent work. The experimental design shown in Figure 1 shows a sample compressed btw the diamond anvils. This is not standard. Even an experiment where a sample is compressed in a gasket between two anvils is quite outdated or restricted to very particular cases such as the rotational DAC that the authors mention in the manuscript.

. Sample thickness profile and pressure-dependence of the yield strength of phases are [SEP]
. 84 determined using X-ray absorption^{4,5,8} and broadening of X-ray peaks^{8,41}. [SEP]

-> Peak width of Debye fringes (I assume that's what the authors refer to when they talk about 'X-ray peaks') depends on strain and grain size. In the experiment that the authors propose grain size would change with load. I would be interested to know how the authors suggest to discriminate grain size statistics from strain.

The method that the authors propose is potentially useful for the study of polycrystalline aggregates under non-hydrostatic compression. Such conditions occur in a variety of experiments and cannot always be avoided (formation of non-quenchable high pressure phases with laser-heating in diamond cells) or are used intentionally in shear-experiments.

Hence, I believe this paper to be useful for the community of high-pressure experimentalists but the

problem that the authors claim to solve is not a general one. I suggest to submit this paper to a more topical journal than Nature Communications.

Reviewer #1 (Remarks to the Author):

This is a very 'solid' report that attempts to bring several simulations and experimental data together to answer a very long standing question regarding the interplay between stresses, plastic strain and pressure measurement. The authors apply it to the long studied (and probably the problem that raises questions with every study) alpha-omega transition in Zr. The current manuscript also tries to evaluate a plethora of studies that are arising out of shear devices like the rotational diamond anvil cell (RDAC). In fact, this study highlights the pitfalls of studies with RDAC that can end up being highly irreproducible since improper characterization of the stress fields leads to improper estimation of pressure. This is highlighted with simulations and careful experimental data on the radial pressure distributions at various peak pressures that are validated by FEM calculations. I have no hesitation in recommending this for publication as is. This research would be followed by many high pressure researchers from as diverse a field as rock mechanics to additively manufactured materials. I do have a few questions for the authors.

Authors' Response:

We greatly appreciate the Reviewer's positive evaluation of our results.

Reviewer's Comment:

(1) A large part of the simulations assume equilibrium conditions (Reuss limit). How sure are the authors that their experiments have actually attained equilibrium? I know they show great equivalence between theory and experiment but I was wondering if this is incidental or global.

Authors' Response:

We use the Reuss hypothesis for the analytical approach only; FEM does not need it. We added on p. 5:

[“This hypothesis appears to work well due to the highly textured polycrystalline aggregate.”](#)

In the limit, when all grains are fully aligned, there is no difference between single and polycrystal, and both Reuss and Voigt hypotheses should work. And yes, the good correspondence between theory and experiment is the main judge of this and other hypotheses for these and many different situations.

Reviewer's Comment:

(2) One of the vexing questions in elastic-plastic deformation studies in a DAC has been the Reuss-Voigt interplay and in the past, there has been discussion on how particle size affects this at high

packing density and shear. Can the authors comment on this especially in view of their CEA approach.

Authors' Response:

We are aware of this discussion. The second Reviewer also raised a question about the effect of the grain size variation on the interpretation of the XRD results. We elaborated our text on p. 4 as follows:

“Importantly, to exclude the effect of strain hardening, change in grain size and dislocation density, and their effect on the thermodynamics and kinetics of PT, we have strongly preliminary deformed Zr until its hardness does not change^{11,35}; grain size and dislocation density in pure α - and ω -Zr do not change with further straining as well⁴⁸.”

Including all these parameters is still possible but requires more advanced modeling and coupling to experiments, which we are working on.

We greatly appreciate the Reviewer's time and efforts in reviewing our paper, useful critical comments, and positive decision.

Reviewer #2 (Remarks to the Author):

Reviewer's Comment:

(1) The authors present a coupled experimental-analytical and experimental-analytical-computational approach for unraveling stress distributions in compression experiments with diamond anvil cells (DAC). The approach may be applied to a) assessing phase boundaries, b) understanding kinetic boundaries in the s.c. rotational DAC, that is: rotational shear experiments with extreme stress gradients.

Authors' Response:

Thank you for the nice summary. We would like to add that this method also allows one to study (a) the plastic flow of various materials under high pressure, (b) the quantitative kinetics of plastic strain-induced phase transformations and chemical reactions, both in DAC and rotational DAC, and (c) initiates high-pressure tribology.

Reviewer's Comment:

(2) The approach is interesting, yet it addresses problems specific to a few types of experiments with the DAC, but it does not apply any longer to DAC experiments in general: The community has turned to compression of single crystal specimens in hydrostatic and nearly hydrostatic media which remove much of the issues addressed by the authors here. Furthermore, Laue diffraction and

multicrystal indexation approaches allow for assessing strain of individual crystallites in polycrystals. The use of nearly hydrostatic media like neon and helium is now common practice.

Authors' Response:

There are no DAC experiments in general. Different designs are used for specific problems, goals, and measurements for hydrostatic and nonhydrostatic experiments. We are aware that there is a community that deeply studies compression of single crystal specimens in hydrostatic and nearly hydrostatic media, utilizing Laue diffraction and multicrystal indexation approaches for assessing the elastic strain of individual crystallites in polycrystals. We communicate with some researchers from this community, trying to find which methods will apply to our problems, and recently have published a joint paper (Nature Communication, 2022, Vol. 13, 982. Here, Laue diffraction alone could not determine the orientation of interfaces between Si I and Si II phases unambiguously; our molecular dynamics and analytical approaches, which showed consistency with the Laue diffraction, resolved this problem and revealed a new nontrivial interfacial nanostructure). It looks like the Reviewer is so deeply, enthusiastically, and successfully involved in this research that he/she missed that numerous other communities lead completely different research driven by practical and fundamental needs. Most engineering materials are polycrystals, and the determination of any property of or processes in a polycrystal based on known properties of and processes in a single crystal (even if we neglect properties of grain boundaries) is a very complex theoretical problem, which is under constant development. Thus, polycrystals should be studied separately, and even when strains of the selected crystallites in polycrystals are measured, this does not give direct answers on the behavior of a polycrystalline aggregate. Also, large communities work on many advanced problems that cannot be studied under hydrostatic conditions. For example, a large geophysical community studies strength and plastic flow under high pressure. A large community uses high-pressure torsion to produce and study nanostructured materials by severe plastic deformations (SPD) and phase transformations. We do the same with traditional and rotational diamond anvils, which allows us to study these processes in situ, combining with FEM simulations. This is unique for nanostructured materials and SPD communities, which is why we are invited to give multiple plenary and keynote lectures at their conferences. The same is true for a large mechanochemical community.

In addition to large communities, there are new emergent directions. For example, contact friction shear stress between diamond and sample/gasket is responsible for generating high pressure, even for quasi-hydrostatic experiments; here, we present the first rules for friction between diamond and Zr. Surface treatment of strong materials (polishing, turning, etc.), deep-focus earthquakes, plastic strain-induced synthesis of (new) materials, the mechanochemical origin of life, etc., involve SPD under high pressure. All of them are mentioned at the beginning and end of the paper, with proper references; all of them cannot be studied under hydrostatic conditions and need methods that we developed in the current paper.

Thus, we do not “address problems specific to a few types of experiments with the DAC;” there are numerous broad problems for which our methods are applicable.

To address the Reviewer’s concern, we added the following text to the paper.

On p. 1:

“We will focus here on stresses and plastic strains averaged over the polycrystalline aggregate rather than in individual grains.”

On p. 2.

“Severe plastic deformation with high-pressure torsion⁴⁵ is an example of the realization of such technologies. Strain-induced PTs under high pressure also occur during surface processing (polishing, turning, scratching, etc.) of strong brittle semiconductors and ceramics and are utilized for developing regimes of ductile machining⁴⁶.”

Reviewer’s Comment:

(3) Ultrahigh compression experiments on simple metals and ruby show that deviations from hydrostaticity are low up to 40-50 GPa, and for most materials tolerable (within +/- 5 GPa) to beyond 100 GPa.

Authors’ Response:

We understand that for the specific goals of those works, such a nonhydrostaticity may be tolerable. But this is not the case for quantitative study of phase transformations. It is known that different pressure-transmitting media, even in the low-pressure range, strongly affect phase transformations, in particular, in Fe [24] and Ti [43], which leads to the large scatter in phase transformation pressures from different works. The problem is not only in nonhydrostatic stresses, but that sample may undergo plastic deformation, leading to a completely different type of phase transformations—strain-induced phase transformations—with completely different thermodynamic and kinetic treatments. There was no way to estimate these effects quantitatively, and our work is the first crucial step toward resolving this general problem. This was written in the concluding part:

“Finding fields of stress tensor components (which can be done using an analytical model) will allow quantifying their effect on the processes under study instead of referring to the qualitative effect of pressure-transmitting media and "non-hydrostatic" stresses. Finding fields of plastic strain tensor components that cannot be measured will allow one to quantitatively study plastic strain-induced PTs and chemical reactions and initiate quantitative high-pressure mechanochemistry.”

Also, ruby shows pressure within a ruby particle, which is different from the pressure in the surrounding sample. The presence of ruby may promote phase transformations by producing a concentration of nonhydrostatic stresses near its surface. That is why we are not using ruby and rely on XRD. A recent Science paper [47], to which we contributed with FEM simulations and general guidance in mechanics, developed a new method to measure normal and shear stresses on the boundary between diamond and pressure-transmitting medium/sample and gasket, again

showing the problem's importance. Our current results are much more ambitious than in [47] because they determine all stress and plastic strain tensor components in the entire sample.

Reviewer's Comment:

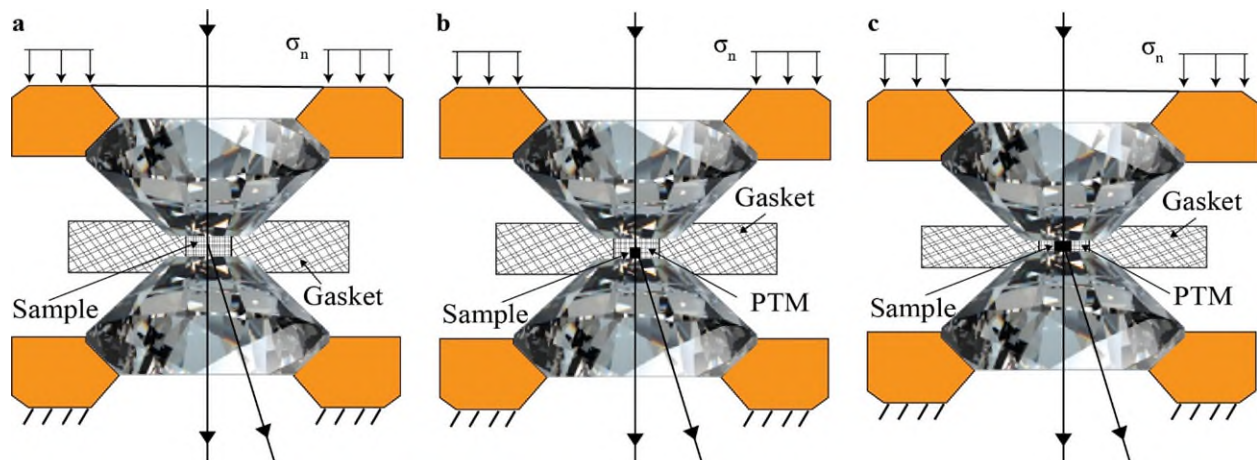
(4) The experiment that the authors show in Fig 1 falls back beyond the diamond cell experiment design that has been established over the past decade.

Authors' Response:

The design that the Reviewer referred to is developed for completely different purposes. Design in **Fig. 1** was used in all previous papers [1,4,5,6,21,32,33] in Science, Nature, and PNAS, devoted to determining radial distributions of pressure, thickness, and determination of the pressure dependence of the yield strength. Such a gamut of publications actually shows that our work is not for a specialized journal. For two-stage DACs (like in [2,3,8,9,10]), which are currently used for ultrahigh pressure studies, despite using neon or helium, the sample is compressed directly by anvils (like in **Supplementary Fig. 12c**), and our approach is directly applicable.

Motivated by the Reviewer, we added the following text in p. 11 and **Supplementary Fig. 12**:

“The same methods are applicable for other material systems (including gasket materials), for sample-gasket systems, without and with hydrostatic medium, after its solidification, and can be extended for processes in rotational DAC (**Supplementary Fig. 12**).”



Supplementary Fig. 12: Schematics of DAC assemblies for which the developed approach is applicable. (a) Solid sample within a gasket without a hydrostatic medium (e.g., like in ref.^{18,19} with FEM simulations in²⁰ or any powder material). (b) Solid sample within a gasket with hydrostatic pressure-transmitting medium (PTM) after their solidification (e.g., like in ref.²¹⁻²⁴). (c) The same as in (b) but after the sample is directly compressed by anvils, from the beginning or above some load (e.g., like in ref.^{18,21,25,26}). All fields in the solidified pressure-transmitting

medium and gasket can be studied in the same experiment. The developed approach can be extended for rotational DAC when torque is applied in (a)-(c).

On p. 1.

“The same happens when the pressure-transmitting medium solidifies (**Supplementary Fig. 12**).”

On p. 2.

It is known that phase transformations (PTs) and chemical reactions strongly depend on the nonhydrostatic stresses and plastic strains^{11,16,20,22,23,26-31,41,42}, **even within different pressure-transmitting media at relatively low pressure^{24,43}**.

Reviewer’s Comment:

(5) The approach proposed by the authors has its merits and is useful for some experiments, but it is not sufficiently general nor do the authors present a case of sufficiently general scientific importance that would justify publication in Nat. Com (the alpha-omega boundary in Zr is now quite well assessed). I recommend the authors to consider a more topical journal like J. Synch. Rad. High Pressure Research, Rev. of Sci. Instr.

Authors' Response:

Thanks to the Reviewer's concerns, we believe that we have now convincingly demonstrated that our approach applies to a very broad class of experiments and scientific problems, important for many scientific communities. The fact that particular cases of the same problem have been published in Science, Nature, Nature Communications, and PNAS [1,2,4,5,6,8,9,21,32,33,47] confirms our statement.

Concerning “the alpha-omega boundary in Zr is now quite well assessed,” please see below.

Reviewer’s Comment:

(6) I add a list of comments jotted down during reading the manuscript, with the hope that they may be helpful for the authors:

'However, they could not be measured. Even measured pressure distribution contains significant error.' (Ref. 9-12)

-> This statement is not quite up to date (nor are the references): Recent Laue diffraction experiments across the phase transition boundary quantify strain. The corresponding stress requires independent assessment of the elastic tensor, of course.

the most advanced characterization of the pressure conditions in a sample is based on determining the radial distribution of pressure averaged over the sample thickness using volume of a crystal cell measured by X-ray diffraction (XRD) and equation of state (EOS) determined under hydrostatic conditions^{4,5,8}.

-> Again, this is NOT the 'most advanced' characterization! Instead, single crystals of either phase should be used or domains of twinned crystals should be indexed. This is well possible in diamond cells. There are new approaches of multicrystal indexation where the UB matrices of each or most grains are assessed - both for white and monochromatic XRD.

Authors' Response:

As we already described above, we are not interested in the fields in each grain under quasi-hydrostatic loading, but rather in the heterogeneous fields in the polycrystalline aggregate under nonhydrostatic compression and plastic flow, in line with the cited literature in this field. These are two independent areas, and they should not be confronted with each other.

Reviewer's Comment:

(7) However, EOS for hydrostatic and nonhydrostatic loadings are quite different⁹⁻¹².

-> A nonhydrostatic loading does not actually give different isotherms, only if non-hydrostatic strain and stress remain unquantified, the isotherms appear to deviate

The authors are aware of this, but the wording is confusing.

Authors' Response:

The elasticity rule is the relationship between 6 components of the stress tensor and 6 components of the strain tensor. Formally, any relationship between traces of these tensors, which are pressure and volumetric strain, must depend on the other five components of these tensors, excluding the unphysical case when volumetric and deviatoric responses are fully uncoupled. That is what was quantitatively discussed in Ref. 12-15. Utilization of the hydrostatic EoS for nonhydrostatic loading was the only reason our paper [11] was rejected from PRL. The same problem was raised at many seminars. This was one of the drivers of why we developed the current method.

Reviewer's Comment:

(8) More importantly, for the XRD beam along the symmetry axis of the DAC (axial XRD), crystallographic planes that are almost parallel to the beam contribute to the measured XRD patterns only, and axial elastic strain $E_{0,zz}$ and consequently stress $\bar{\sigma}_{zz}$ do not contribute to the pressure, leading to large error (bar over the field variables means averaged over the sample thickness). In addition, numerous physical, chemical, geological, and mechanical

-> This is true for non-hydrostatic experiments. The alpha-omega transition in Zr is at a pressure that is well within a regime where hydrostatic pressure can be achieved with neon or helium as pressure-transmitting media in a diamond anvil cell. The authors are referring to problems specific to non-optimal experiments or outdated approaches. The authors' approach is useful for analysing data obtained with the s.c. rotational DAC.

Authors' Response:

The maximum hydrostatic pressure at room temperature that can be achieved with He before it solidifies is 12.1 GPa. For higher pressure, the experiment is always nonhydrostatic, which may be tolerated by some communities for some problems and not accepted by other communities working, e.g., on phase transformations. Formally, hydrostatic loading is a very particular case of general loading under the action of all 6 components of the stress tensor and also plastic strain tensors, so our approach is much more general and requires completely different treatments. But of course, it is not needed for pure hydrostatic and close-to-hydrostatic experiments, for which completely different and very important problems are being solved. So, these are completely different fields, which should not be confronted, and we completely and respectfully disagree with the Reviewer's statement about the "non-optimal experiments or outdated approaches."

Yes, the alpha-omega transition in Zr is well studied under hydrostatic pressure, and we use these data (EOS of phases, transformation pressure, and elastic constants) as input data in our approach. But this is only the second paper after [11] on in situ quantitative study of any plastic strain-induced phase transformation, with very different interpretations due to coupling to the theory and FEM simulations. The Reviewer considers nonhydrostaticity as an undesirable effect. As we stressed in the paper and the above responses, numerous problems and processes intentionally involve a combination of high pressure and large plastic deformations, which must be studied. In particular, many dozens of papers study the production of nanograined alpha and omega Zr and their nanocomposite (and many thousands of papers for all other possible materials) by high-pressure torsion. As mentioned above, since we study the same grain refinement and phase transformation process in traditional and rotational DAC in situ, this work attracts significant interest from this large SPD community. Also, we showed that after reaching steady hardness and microstructure, phase transformation pressure is the same in traditional and rotational DACs, which has several consequences. First, for DAC experiments involving plastic deformations, the phase transformations are plastic strain-induced (rather than pressure-induced), which required completely different thermodynamic and kinetic treatment and experimental characterization. Second, one can study nanostructure formation and phase transformation under severe plastic deformations not only in rotational but also in traditional DAC. Of course, rotational DAC allows much broader loading paths, especially at low pressures, which is important for both fundamental and practical applications.

As Reviewer can see in our paper, the alpha-omega phase transformation pressure determined with the developed CEA-FEM approach for plastic strain-induced transformation is 2.7 GPa, 2 times lower than under hydrostatic conditions and even 1.3 times lower than the phase equilibrium pressure, and it is essentially different from 1.36 GPa, which we found based on known EOS method. This pressure is found to be independent of the plastic strain tensor and its path,

particularly of the compression-shear strain path. The kinetics of transformation is completely different than under hydrostatic conditions: time is not a parameter, and plastic strain plays a role of the time-like parameter. The theoretically predicted plastic strain-controlled kinetic equation was verified and quantified; it is found to be independent of the plastic strain at pressures below the initiation of PT and pressure-plastic strain loading path.

These are the first new rules in the relatively new field of plastic strain-induced phase transformations, which has numerous practical applications. Zr is just the first material we study; the same methods apply to any material at much higher pressure, including megabar pressure.

Reviewer's Comment:

(9) The only paper that claims measurement of radial distribution of all components of the stress tensor is ref. 40.

-> I don't understand this statement. There are numerous published studies on samples compressed in diamond cells under hydrostatic conditions, i.p. on single crystals. This includes studies where elastic tensors were measured with Brillouin spectroscopy along with single crystal diffraction data or axial compressibilities were assessed from single crystal compression data.

Authors' Response:

As we already discussed and stressed in the paper, this paper is not about hydrostatic pressure (which does not have distributions because it is homogeneous), single crystals, and elastic moduli. But we use and cite data obtained under hydrostatic pressure and elastic moduli of a Zr single crystal in our simulations.

Reviewer's Comment:

(10) The authors address a problem of specific experiments and samples, it is not a general problem and it appears the authors are not aware of much of the recent work. The experimental design shown in Figure 1 shows a sample compressed btw the diamond anvils. This is not standard. Even an experiment where a sample is compressed in a gasket between two anvils is quite outdated or restricted to very particular cases such as the rotational DAC that the authors mention in the manuscript.

Authors' Response:

We have already addressed this many times, added **Supplementary Fig. 12** with additional designs, and recent references from Nature and Nature Communications journals showing problems for which our method is important.

Reviewer's Comment:

(11) Sample thickness profile and pressure-dependence of the yield strength of phases are determined using X-ray absorption^{4,5,8} and broadening of X-ray peaks^{8,41}.

-> Peak width of Debye fringes (I assume that's what the authors refer to when they talk about 'X-ray peaks') depends on strain and grain size. In the experiment that the authors propose grain size would change with load. I would be interested to know how the authors suggest to discriminate grain size statistics from strain.

Authors' Response:

This is a very important point, and we carefully thought about it. We elaborated our text in p. 4 as follows:

“Importantly, to exclude the effect of strain hardening, change in grain size and dislocation density, and their effect on the thermodynamics and kinetics of PT, we have strongly preliminarily deformed Zr until its hardness does not change^{11,35}; grain size and dislocation density in pure α - and ω -Zr do not change with further straining as well⁴⁸.”

Including all these parameters is still possible but requires more advanced modeling and coupling to experiments, which we are working on.

We also added in “MATERIAL AND EXPERIMENTAL METHODS” Section on p. 12:

“Based on the different angular dependence of the grain size and microstrain contributions to the diffraction peak broadening, they can be separated. The whole powder pattern fitting using the modified Rietveld method (as implemented in MAUD software⁵⁸) was utilized, which takes texturing and stress anisotropy into account.”

Reviewer's Comment:

(12) The method that the authors propose is potentially useful for the study of polycrystalline aggregates under non-hydrostatic compression. Such conditions occur in a variety of experiments and cannot always be avoided (formation of non-quenchable high pressure phases with laser-heating in diamond cells) or are used intentionally in shear-experiments.

Hence, I believe this paper to be useful for the community of high-pressure experimentalists but the problem that the authors claim to solve is not a general one. I suggest to submit this paper to a more topical journal than Nature Communications.

Authors' Response:

We greatly appreciate the Reviewer's time and efforts in examining our paper and challenging critical comments. We took the Reviewer's comments very seriously and added new content to the text and figures. We also described our arguments to the Reviewer about the broadness of the problems that can be treated by our methods, including citing papers from Science, Nature, Nature Communications, and PNAS.

The first Reviewer is very positive about our paper and wrote, “answer a very long standing question regarding the interplay between stresses, plastic strain and pressure measurement” and “This research would be followed by many high pressure researchers from as diverse a field as rock mechanics to additively manufactured materials.”

The current Reviewer did not criticize our specific methods and results. He/she wrote, “The approach is interesting” and “The method that the authors propose is potentially useful for the study of polycrystalline aggregates under non-hydrostatic compression. Such conditions occur in a variety of experiments and cannot always be avoided (formation of non-quenchable high pressure phases with laser-heating in diamond cells) or are used intentionally in shear-experiments. Hence, I believe this paper to be useful for the community of high-pressure experimentalists ...”

The only problem is that the Reviewer is so deeply, enthusiastically, and successfully involved in this research that he/she missed that various completely different large communities lead completely different research driven by practical and fundamental needs, which are addressed in our paper. We would like the Reviewer to imagine that he/she submitted the unique results with Laue diffraction under hydrostatic pressure with strains in selected grains and will get a review that this is not general, and the community has turned to time-resolved dynamic experiments under much higher pressure or to study of the polycrystalline aggregates under general 6 components of the stress and plastic strain tensors. Fighting between different fields will not help in the development of science.

We addressed this misunderstanding in detail and hope the Reviewer will show the broad-mindedness corresponding to his/her high-level status and accept our arguments.

REVIEWERS' COMMENTS

Reviewer #1 (Remarks to the Author):

The authors have answered all my queries and doubts and modified the MS accordingly to reflect my comments. I feel that the MS can be published as is.

Reviewer #2 (Remarks to the Author):

the paper has been revised and addresses all comments of the reviewers. I think this work is technically sound.